Title: Global quantitative understanding of nonequilibrium cell fate decision making in response to pheromone

Authors: Sheng Li [1,2], Qiong Liu[2]*, Erkang Wang [1,2], Jin Wang[3]*

Affiliations:

[1]College of Chemistry, Jilin University, Changchun, Jilin, 130012 P. R. China.

[2]State Key Laboratory of Electroanalytical Chemistry, Changchun Institute of Applied Chemistry, Chinese Academy of Sciences, Changchun, Jilin, 130022, China.

[3]Department of Chemistry and of Physics and astronomy, State University of New York at Stony Brook, Stony Brook, New York, 11794-3400, USA.

*Corresponding author. Email: liuqiong@ciac.ac.cn; jin.wang.1@stonybrook.edu.

Abstract:

Cell cycle arrest and polarized cell growth are commonly used to qualitatively characterize the fate of yeast in response to pheromone. However, the quantitative decision-making process underlying the time-dependent changes in cell fate remains unclear. Here, by observing the multi-dimensional responses at the single-cell level experimentally, we find that yeast cells have various fates. Multiple states are revealed, along with the kinetic switching rates and pathways among them, giving rise to a quantitative landscape of mating response. We developed a theoretical framework using a nonequilibrium landscape and flux theory to account for the cell morphology observed experimentally and performed a stochastic simulation of biochemical reactions to explain the signal transduction and cell growth. Our experimental results established the first global quantitative demonstration of the real-time synchronization of intracellular signaling with their physiological growth and morphological functions which reveals the underlying physical mechanism. This study provides an emerging mechanistic approach for understanding the nonequilibrium global pheromone-regulated cell fate decision-making in growth and morphology.

Keywords:

Mating pathway; Cellular fate decision-making; Landscape; Flux; Nonequilibrium.

Main Text:

INTRODUCTION

Facing a variety of external stimuli, cells integrate information from various sources and initiate appropriate stress responses, such as survival or death, division or differentiation, and shape change or migration (*1-11*). To better understand the cellular response to external stimuli, we chose the pheromone pathway of *Saccharomyces cerevisiae*, which is a classical model of the mitogen-activated protein kinase (MAPK) signaling pathway (*12-15*). *Saccharomyces cerevisiae* has two modes of reproduction, sexual mating reproduction and asexual budding reproduction (*16-20*). These two reproductive modes can be converted either with or without the assistance of external pheromone stimulation from a partner (*21*). For sexual reproduction, mating to form a diploid cell is the natural behavior of heterosexual haploid *Saccharomyces cerevisiae* to cope with an unfavorable environment and to improve their survival rate for generations (*22-24*). Pheromones, a type of sex hormone secreted by *Saccharomyces cerevisiae*, serve as the yeast's mating signal, informing its partner to prepare for the beginning of cell fusion. (*22-30*). What will happen to the yeast cell if its partner does not arrive and this normal stimulation continues? From microscopic gene network **(Fig. 1)**, external signals are transmitted to Fus3 through a series of internal proteins such as prototype heterotrimeric GTP binding protein and the MAPK kinase cascade (*31-33*). Then, Fus3 shuttles back and forth across the nuclear membrane, directly or indirectly activating genes for cell cycle arrest (Far1) and polar growth (Bni1) (*34-42*). Thus, the current understanding of the pheromone-induced fate of yeast cells can be qualitatively summarized as the occurrence of cell cycle arrest and polarized cell growth (*43-45*).

While studying qualitatively the fates of cells, researchers realized that, in the presence of many potential external stimuli, the decision-making of the cells can play a central role in the fates of the cells (*46-55*). Biologically, the cell fate decisions can also be qualitatively described by the cascading transmission of the signals along a static causal pathway (*56-60*). However, it is unknown how cell fate decision-making evolves quantitatively over time during the global response at both the mesoscopic and microscopic level. Since the living cell itself is a complex non-equilibrium micro system, disturbances of the external environment undoubtedly disrupt the original balance of the yeast cells and exacerbate the imbalance of the internal activities (*61-70*). However, quantifying these underlying cell fate decisions in response to external stimuli remains a significant challenge.

Indeed, from a microscopic perspective, the cellular decision-making of yeast in response to mating information is accomplished through multiple feedback loops (**Fig. 2A**), not only including the positive feedback regulation mediated by Fus3, but also through certain negative feedback regulation that can effectively reduce the transcriptional output of this pathway (*71-76*). After pheromone stimulation, there are two pathways that can lead to polar growth of the cells (**Fig. 1**). The first path (P_1) is "Fus3 → Far1/Cdc24 → Cdc42 → Bni1" (*44, 77-80*). This is realized by Fus3 entering the nucleus to activate Far1, which can escape from the nucleus to activate Bni1 indirectly. The second path (P_2) is direct activation by Fus3 of Bni1 in the cytoplasm, "Fus3 → Bni1" (*35, 81*). In the process of these two polar growth pathways acting alone or in concert, the pheromone-induced self-activation of Fus3 ("Fus3 → Fus3") facilitates the rapid transmission of the signals (*82-85*). Activation of the pheromone pathway also induces multiple negative feedback loops, such as I_1 (Sst2 and Gpa1) (*74-76, 86-88*), I_2 (Msg5 and Bni1) (*35, 72-76, 89-91*) in the pathway. Only at high-dose pheromone levels is the negative feedback of the downstream Msg5

upregulated (*72*) and only at high concentrations of Bni1 is activity of Fus3 indirectly reversed by Bni1 (*35, 81, 92-94*).

Here, by observing the multi-dimensional response at the single-cell level, we discovered the non-equilibrium steady states, which demonstrate the cell fates quantitatively, in response to different concentrations of pheromone. These steady states or cellular destinies include two gene expression levels, four growth rates, and four morphological fates. We quantified these responsive fates of the yeast cells in real time from various dimensions, including expression levels of Fus3 inside and outside of the nucleus, cell morphology, cell growth rate, and the stimulation concentrations. Multiple states, as well as switching kinetic rates and pathways among them, were revealed, giving rise to a quantitative landscape of the mating response. The applications of landscape and flux theory to this biological system enabled us to quantify the non-equilibrium dynamics of the yeast cell mating responses. Our results established a global and physical framework for understanding cell fate decision making and mating dynamics. Furthermore, we experimentally validated the proposed molecular mechanism for the formation of these states. These molecular mechanisms establish the links between molecular events to cellular characteristics across scales. They allow for the real-time synchronization of intracellular signaling with their physiological growth and morphological functions, bridging microscopic mechanisms and mesoscopic functions. To further elucidate these microscopic mechanisms, we conducted biochemical reaction simulations to demonstrate the emergence of these states. These findings shed new light on the global signaling mechanisms that govern how yeast determines its cellular fate in response to pheromone.

RESULTS

Quantifying the cellular decision-making threshold

Studies have shown that yeast, for which mating decisions are an all-or-none switch-like response, can automatically filter out very low-dose pheromone signals and only respond near a critical concentration or higher (*88, 95, 96*). This is due to the fact that very low doses of pheromone induce insufficient accumulation of intracellular signals, such as Fus3, which are incapable of initiating the mating-readiness project (*97-99*). To determine a pheromone concentration capable of arresting the cell cycle, we measured the fluorescence intensity of *FUS3*-GFP by flow cytometry in yeast cells incubated for 24 h with varying pheromone concentrations **(Fig. 2A)**. According to the fitted statistics, the expression of Fus3 at a pheromone dose of 0.01–0.4 μM showed unimodal distribution of the fluorescence intensities. The bimodal distribution representing the bistable states gradually began to appear when the dose was about 0.6 μM.

In order to comprehend the correlation between gene expression levels of Fus3 and the threshold of cellular response, the fluorescence intensity trajectories of Fus3 expression in single cells were associated with the microscopy-based cellular response under various pheromone concentrations over time. A microfluidic device was used to culture yeast under constant temperature conditions in real time. Using total internal reflection fluorescence microscopy, the survival status and fluorescent signals of the yeast cells were captured in real time **(Movies S1–S7)**. Compared to 0.7 μM pheromone, the expression of Fus3 in the yeast cells did not fluctuate significantly at 0.2 μM, resulting in its inability to inhibit cell budding reproduction **(Fig. 2B)**. However, the expression of Fus3 at a pheromone concentration of 0.7 μM exhibited four stages: the initial stage (0–b_1), the adaptive stage (b_1–b_2), the stable stage (b_2–b_3), and the recovery stage (b_3–b_4), corresponding to the biological behavior of yeast cells at different stages. Therefore, the

unimodal distribution of 0.01–0.4 μM pheromone occurred when only the initial cells (0-b_1) were present in the flow cytometer sample. This very low dose of pheromone was unable to arrest the cell cycle from the beginning in yeast. If the pheromone had arrested the cell cycle of yeast cells from the beginning, but not for more than 24 h, some yeast cells would have resumed budding at a later stage. As demonstrated by the bimodal distribution of 0.4–1.5 μM pheromone, the sample contained yeast cells in two distinct states (b_2–b_3 and b_3–b_4).

The results measured by flow cytometry were only rough estimates of critical mating decision thresholds, whereas microscopy of individual cells cultured in microfluidics revealed more precise cellular decisions. During culturing with varying concentrations of pheromone, we found that the time required for yeast cells to arrest their cell cycle was directly proportional to the pheromone concentration **(Fig. 2C)**. By extending the duration of the pheromone stimulation, the yeast cells gradually adapted to the external surroundings and resumed budding reproduction.

Two cell fate decision states reflected in the expressions of Fus3

To explore the yeast cell fate decision-making during the stable stage (b_2–b_3 in **Fig.2B**), the fluorescence intensity trajectories of Fus3 inside and outside the nucleus were plotted over time **(Fig. 3A and Fig. S1–S2)**. The trajectories demonstrated that after approximately 600 min of yeast cell cultivation, Fus3 entered a stable stage where its fluorescence fluctuated around a certain value. In non-equilibrium statistical physics, the fluorescence intensity curve in this stable stage can be interpreted as a non-equilibrium steady state, whereas the rising phase of the first 600 min can be interpreted as a non-equilibrium non-steady state, or the relaxation process of the response. To visualize the cell fate of yeast at the level of gene expression, the three-dimensional statistical distribution of Fus3 (cytoplasmic and nuclear fluorescent signals) was plotted during the non-equilibrium steady-state phases **(Fig. 3B and Fig. S3–S5)**. Clearly, the landscape of Fus3 displayed two peaks, which correspond to the two cell fates that existed both inside and outside the nucleus.

To comprehend the logical relationship between the cell fate at expression levels of Fus3and pheromone-influenced signaling in the transduction process, we explored the biological mechanism underlying the emergence of these two Fus3 fates. We proposed that the two fates of Fus3 expression observed in signaling could be explained by a logical sequence involving functional depletion and feedback loops. First, functional depletion means that when the amount of Fus3 in the nucleus was sufficient to arrest the cell cycle and activate the mating protein ("$\mathrm{Outer_P_1} \rightarrow \mathrm{Far1}\ \&\ Ste12$"), the excess Fus3 was transported out of the nucleus for polar growth ("$\mathrm{Outer_P_1} \rightarrow \mathrm{Inner_P_1}$" and "$\mathrm{Inner_P_2} \rightarrow \mathrm{Outer_P_2}$") **(Fig. 3C)**. Second, the feedback loop means that yeast actively regulated Fus3 expression by activating or inhibiting signals. Previously, experimentally validated feedback loops were categorized into two models: "A → Fus3 ┤ A" focuses primarily on the pathways involving Gpa1 and Sst2, whereas "Fus3 → B ┤ Fus3" focuses primarily on the pathways involving Ste12 and Msg5 **(Fig. 1 and Fig. 3D)**.

This dynamic sequential mechanism results in two behaviors: the highly coordinated expression levels of Fus3 inside and outside the nucleus, and the alternation of the two fates. As experimental evidence for our proposed molecular mechanism, we observed the existence of two behaviors. We revealed a correlation between intra- and extra-nuclear fluorescence intensities using Pearson's coefficient. A linear correlation of approximately 0.80 between these two types of fluorescence trajectories at various pheromone concentrations indicated a strong synergy between them **(Table 1)**. In addition, using a hidden Markov chain model, we characterized the two cellular fates using gene expression levels by fitting the fluorescence trajectories into high states ($\mathrm{H_1}$, $\mathrm{H_2}$)

and low states (L_1, L_2) **(Fig. 3E)**. The fitted red line in **Fig. 3E** demonstrates that the two trajectory fates (high and low states) inside and outside the nucleus could switch to each other, supporting our logical interpretation of the state switching above.

Uncovering the physical characteristics of cellular decision-making landscapes

To uncover the physical characteristics of the underlying bistable landscapes, we employed a Hidden Markov Chain model to compute the transition probability, transition rate, and residence time between the two gene expression fates. In the non-equilibrium steady state, the steady state probability can be used to quantify the population landscape P or the potential landscape U (*68, 100-102*), where U is defined as the negative logarithm of the steady state distribution P of gene expression, $U = -\ln P$. As can be seen, the population and potential landscapes (P and U) at various pheromone concentrations have two basins of attractions that are separated by barriers **(Fig. 3B and Fig. S3–S5).** The transition probabilities and residence times of the two expressions of *FUS3*, high state (H_1, H_2) and low state (L_1, L_2), can be determined through the statistical analysis of the experimental data fitted by the hidden Markov chain model. The transition rate can be derived from the transition probability, whereas the barrier height is determined by fitting two peaks into the landscape. The barrier height is determined by the depth of the basin on the potential energy landscape ($U = -\ln P$) obtained directly from the statistical histogram (P) of the fluorescence signals of the gene expressions **(Table 2)**.

At pheromone concentrations between 0.7 μM and 0.8 μM, the barrier heights of the low state (L_1, L_2) were less than those of high state (H_1, H_2), whereas the opposite was true between 1.0 μM and 3.0 μM **(Fig. 4A)**. In physics, the transition between steady states becomes harder as the barrier height increases, resulting in a longer residence time (*100, 103*). According to the statistical results of the experimental data, the distribution of high and low states of residence times in different pheromone concentrations is consistent with the distribution of residence times **(Fig. 4B)**. The correlation coefficient between barrier heights and residence times for all concentrations was 0.8806, indicating that they were significantly positively correlated **(Fig. 4C)**. This substantiates the statistical non-equilibrium physics claims regarding barriers and residence time.

To explore the biological implications of the landscape physical characteristics, we calculated the distribution of their ratios for two gene expression fates as a function of pheromone concentration. The opposite trend of the transfer rate ratio (k_{21}/k_{12}) relative to the barrier height ratio or the residence time ratio (high/low, H/L) in response to changes in pheromone concentration indicated that transition rates were lower the deeper the attraction basin **(Fig. 4D)**. To better comprehend this relationship, the potential landscape topographies under varying pheromone concentrations were illustrated **(Fig. 4E)**. Compared to a pheromone concentration of 0.7 μM, 0.8 μM had a deeper attraction basin for its high state than for its low state, making the transition from low to high states easier than that from high to low states. The yeast's cellular decision-making at the level of gene expression was consequently more likely to remain in the high state than in the low state. At 1.0–3.0 μM, the attraction basin of the low state was deeper than that of the high state, leading to the yeast's preference to remain in the low state. In general, as pheromone doses increase from low to high, the basin of the high state gradually becomes shallower, whereas the basin of the low state gradually becomes deeper. The increased height of the low-state potential barrier is due to the negative feedback regulation that is able to inhibit the expression of Fus3, resulting in a greater number of yeast cells in a low-expression state. This supports the biological notion that high-dose pheromone elicits a stronger negative feedback response compared to the low-dose pheromone.

Quantifying the cellular deformation rate in polar growth

Upon observing the polar growth of yeast cells in real time via microscopy, we noticed that the rate of cell deformation did not vary uniformly over time. Meanwhile, except for the top, other parts of the cell changed slightly as the yeast stretched forward **(Movies S3–S7)**. To accurately measure the spatiotemporal change rate of the cell morphology, we used a circular filling pattern to segment the yeast cells **(Fig. 5A)**. To quantify the various cell deformations that occur during cell growth, we considered a value (H_n) comparable to the harmonic mean to characterize the cell morphology. H_n equals the sum of the reciprocal radii of the filled circles multiplied by the number of filled circles, i.e., $H_n = n(\frac{1}{R_1} + \frac{1}{R_2} + \ldots + \frac{1}{R_n})$. The significant advantage of this parameter is that it is particularly sensitive to small morphological changes at various locations of the cell, allowing differential non-directional polar growth and directional normal growth (i.e., lateral growth and longitudinal growth) to be characterized in real time.

From the real-time trajectory of the changes in the cell morphology, as measured by the H_n of the cell-filled circles, we found that there were roughly four types of cell shape changes. According to the definition of H_n describing the cell morphology, the rising phase ($t_1 - t_2$) of the curve primarily represents the change in cell length, whereas the falling phase ($t_3 - t_4$) primarily represents the change in cell width. At the ($t_2 - t_3$) and ($t_4 - t_5$) phases, the slopes of the two curves are close to zero, indicating that cell morphology changes were minimal or nonexistent **(Fig. 5B)**. We collected the statistics on the distribution of the cell growth rates or deformation rates **(Fig. 5C and Fig. S6)**. When the positive and negative values were differentiated, it was evident that the cell growth rate could be divided into four states: the lateral-fast rate (WF), the longitudinal-fast rate (LF), the lateral-slow rate (WS) and the longitudinal-slow rate (LS). Among them, L and W represented the presence and absence of direction in cell deformation, or the length and width, respectively. F and S represent the magnitude of the "driving force" in cell deformation, or the fast and slow growth rates, respectively.

To explore the molecular mechanisms underlying these four growth rates, we took both the direction (L and W) and force (F and S) of cell growth into account. Many studies have shown that Fus3 and Far1, which determine the direction of cell growth along its long axis, are essential genes for bud formation during polar cell growth, and their absence results in mis-localization of shmoo projections (*77, 78, 80, 81, 104*). Thus, the indirect pathway (P_1: "Fus3 → Far1/Cdc24 → Cdc42 → Bni1"), which is more directional than the direct pathway (P_2: "Fus3 → Bni1"), is the leader signaling pathway for longitudinal cell growth. Given that the P_1 pathway requires the sequential activation of multiple proteins and that proteins such as Fus3, Far1, and Cdc24 must be transported into or out of the nucleus, we proposed that the P_2 pathway had a quicker response speed to stimulate cell growth than did the P_1 pathway (**Fig. 5D**). Consequently, the temporal delay in the actions of these two pathways resulted in P_2-dominated undirected growth (model W: P_2), followed by the two growth pathways co-stimulating the cell's polar growth (model L: P_1+P_2) once the P_1 pathway was fully functional. In addition, we proposed that F and S corresponded to the high and low states in Fus3, respectively. When Fus3 was at a high state (H_1, H_2), there was enough Fus3 to stimulate growth (model F). Following entry into the low state (L_1, L_2), only a relatively small amount of Fus3 was available for polar growth (model S).

To confirm that there was indeed a time lag in multi-level protein signaling, we constructed a dual fluorescence system (*CDC24*_GFP-*FUS3*_RFP strain), in which *CDC24* was linked to the green fluorescent protein (S65T) and *FUS3* was linked to the red fluorescent protein (yomCherry) **(Fig. 5E and Movies S8–S9)**. Taking into account the order of signal transduction in yeast in

255 response to pheromone, the expression levels of Fus3 and Cdc24 would achieve the highest degree
256 of correlation or match after a certain time lag. Using a cross-correlation function, we analyzed the
257 in- and out-of-nucleus fluorescence trajectories of Fus3 and Cdc24 to compare the lag times of
258 various activation sequences **(Fig. 5F)**. The figure shows that the lag time between Fus3 in the
259 nucleus and Cdc24 (red curve) reaching a maximum correlation was approximately 120 min, while
260 the lag time between Fus3 outside the nucleus and Cdc24 (blue curve) reaching a maximum
261 correlation was approximately 300 min. The fact that the lag time of Fus3_in and Cdc24_in/out
262 (red curve) in the figure was shorter than that of Fus3_out and Cdc24_in/out (blue curve) confirms
263 the existence of a temporal delay effect in multi-level signaling and provides direct evidence for
264 the temporal distinction in the functioning of the two growth pathways.
265 By taking the growth rate absolute value, we divided the four states into fast growth rate and
266 slow growth rate categories **(Fig. 5G and Fig. S7)**. To confirm that the two forces (F and S)
267 corresponded to the high and low states of Fus3, respectively, the cell growth rate states and Fus3
268 gene expression states were measured as the cell polar growth changed over time. According to
269 the proportion of statistics in the figure, the High (expression) state was primarily contained within
270 the Fast (growth) state, whereas the Low (expression) state was primarily contained within the
271 Slow (growth) state **(Fig. 5H and Table 3)**. Consequently, this also provided quantitative
272 experimental evidence for the cellular growth rate molecular mechanism.

273 **Quantifying the four morphological fates and the phase transition trend**

274 The morphological trajectory of the cell shape over time as described by H_n fluctuated
275 continuously within a given range **(Fig. 5B)**. Using a hidden Markov chain model to fit the time-
276 varying trajectories of cell morphology, yeast cells at different pheromone concentrations
277 exhibited four distinct morphological fates. These four morphological fates corresponded
278 statistically to the four peaks in the distribution of all cell shapes (F_1–F_4) **(Fig. 6A and Fig. S8)**.
279 Due to the fact that H_n is a parameter that is extremely sensitive to changes in the size and number
280 of filled circles within the cell, minute variations in the length or width of a portion of the cell
281 observed through a microscope can result in the cell being classified as having a different
282 morphological fate **(Fig. 6B)**. We proposed, on the basis that cell morphology is an accumulation
283 in growth, that the molecular mechanisms underlying the formation of the four morphological fates
284 were dependent on the different capacities of cells to grow laterally and longitudinally. To test the
285 claim that four morphological fates were formed, the synergistic effect of growth ability in both
286 directions was calculated. The lateral growth capacity of cells was expressed by the rate of change
287 of the average radius of the filled circle within the cell, whereas the longitudinal growth capacity
288 was expressed by the rate of change of the sum of the radii of the filled circle. The existence of
289 four distinct states in the cooperative distribution of the two data, as depicted in the figure, strongly
290 suggested that the capacity to grow in different directions is a crucial factor in determining cell
291 morphology **(Fig. 6C and Fig. S9)**.
292 Notably, a phase transition trend from four states to a dominant state in the cell morphology
293 distribution between 0.7 μM and 3.0 μM was revealed (**Fig. 6A**). Moreover, the morphology of
294 the cells observed under a microscope at a concentration of 3.0 μM was significantly smaller than
295 that observed at other concentrations **(Fig. 6B)**. By measuring the average cell length, it is possible
296 to conclude that a high-dose pheromone concentration (3.0 μM) disrupted the monotonic linear
297 trend observed at low doses (0.7 μM-2.0 μM) **(Fig. 6D and Table 4)**. The microscopic explanation
298 of this phase transition trend is the enhancement of negative feedback regulation under high doses
299 (I_2), suppressing the second polar growth pathway (P_2) **(Fig. 1 and Fig. 3C)**. Three-quarters of the

cell fates (with the exception of F_2) showed a sudden reduction in morphology at a high pheromone dose (3.0 μM), most likely attributed to this impaired P_2 function **(Fig. 6A and Fig. S8)**.

To explain the physical mechanism of the phase transition trend that occurs at high dose (3.0 μM), we quantified the degree of nonequilibrium in the cellular morphological system using the net flux. From the cell morphological trajectories analyzed by the hidden Markov chain model, we determined the transition probability between various cell morphologies. The sum of the three net fluxes, which was obtained by decomposing the probability loops in the transition matrix, was used to represent the degree of the detailed balance collapsed in the cellular morphological system **(Fig. 6E)**. As the concentration of pheromone increased, the intensity of the net flux decreased first and then increased, exhibiting a significant phase transition trend at 3.0 μM. Since the net flux is rotational due to its steady state nature under local probability conservation, it tends to destabilize the point attractors. Therefore, the significant changes in net flux can lead to the instability of the cell attractor states, giving rise to possible phase transition trend. The quantification of this non-equilibrium dynamic explains the physical mechanism by which the phase transition trend in a morphological system was caused by the enhanced capability of the yeast cells negative feedback regulation at high doses.

Simulations for the signal transduction and the cell growth

Based on the functional and quantitative regulation obtained from databases, such as KEGG (Kyoto Encyclopedia of Genes and Genomes, https://www.kegg.jp/), SGD (the *Saccharomyces* Genome Database, https://www.yeastgenome.org/) and EVEX (http://evexdb.org/), we developed a simplified model of signal transduction in the context of global gene regulatory networks **(Fig. 1, Fig. 6F)**. This model simulated a series of biochemical reactions with the Gillespie algorithm (*105-107*) **(Table S6–8)**. By simulating the biochemical reactions associated with the pheromone pathway in yeast cells, the expression levels of Fus3 and the distribution of cell morphology were determined. Fus3 gene expression obtained from biochemical reaction results displayed a two-state distribution inside and outside of the nucleus, validating our understanding of the molecular mechanism underlying the bimodal fluorescence state within the context of the global response **(Fig. 6G)**. Meanwhile, the Bni1 produced by the reactions simulated the dynamic process of cell growth. Although both the growth pathways (P_1 and P_2) were involved in the process of cellular length and width growth, the relative weights of the pathways that grew in the two directions were significantly different. Therefore, we simply defined Bni1_in produced by the P_1 pathway that plays a major role as the longitudinal growth and Bni1_out produced by the P_2 pathway as the lateral growth.

In this simulation, a denotes the longitudinal length of the yeast cell, while b denotes the lateral length of the yeast cell **(Fig. 6F)**. Each iteration increased the longitudinal and lateral lengths of the yeast cells by $\Delta\mathrm{a}$ and $\Delta\mathrm{b}$, respectively. $\Delta\mathrm{a}$ is proportional to "$\mathrm{PBni1_in}$" and inversely proportional to b; $\Delta\mathrm{b}$ is proportional to "$\mathrm{PBni1_out}$" and inversely proportional to a. That is, $\Delta\mathrm{a} = \frac{\mathrm{r_a(PBni1_in)}}{\mathrm{b}}$, $\Delta\mathrm{b} = \frac{\mathrm{r_b(PBni1_out)}}{\mathrm{a}}$. The value N corresponds to the rounding operation of $\frac{\mathrm{a}}{\mathrm{b}}$, i.e., $\left[\frac{\mathrm{a}}{\mathrm{b}}\right]$, and c represents the amount remaining after rounding. The $\mathrm{H_n}$ is $(\mathrm{N}+1)(\mathrm{N/b}+1/\mathrm{c})$. As predicted by the simulation of the cell growth process, the distribution of cell morphology revealed four distinct fates, which corresponded to the experimental observations **(Fig. 6H)**.

DISCUSSION

In this study, we quantitatively uncovered and interpreted the yeast cell fate decision-making in response to pheromone using biological and physical methods. Using flow cytometry, we examined the induction of yeast cells by different concentrations of pheromone to determine the critical threshold for eliciting a cellular response. The purpose of the fitting curve in **Fig. 2A** was to estimate the pheromone dose by determining at what concentration the expression of Fus3 exhibited double peaks. Continuous microscopy observations of *FUS3*-GFP strain yeast cells provided us with a microscopic and mesoscopic view of how the cells responded to pheromone. The four stages of Fus3 expression levels at a 0.7 μM pheromone concentration accurately depicted the mesoscopic cell behavior of cell cycle arrest and polar growth (**Fig. 2B**). Among them, the Fus3 expression levels in the stable stage (b2–b3) fluctuate around a fixed value, which was considered a non-equilibrium steady state period. As our subsequent analysis centered on the non-equilibrium steady-state phase, we chose five pheromone concentrations as stimuli that allowed the yeast cells to maintain a stable-state phase for a sufficient amount of time.

To explore the fate of Fus3 gene expression in a non-equilibrium steady state, we chose data that, after 600 min, brought all the cell fluorescence trajectories into stable-state phase **(Fig. 3A)**. The two fates of Fus3 that resulted from cellular decision-making were separated by the Markov fitting of the trajectories **(Fig. 3B)**. The criterion for data fitting is the probability that the fluorescence intensity at a particular moment in the trajectory belonged to a high state (H_1, H_2) or a low state (L_1, L_2) multiplied by their respective transition probabilities **(Fig. 3E)**. Consequently, there was a chance that the value of the fluorescence intensity in the low state was greater than the value of the fluorescence intensity in the high state. We proposed that the two fates of Fus3 expressions observed in signaling were explained by a logical sequence of point-to-point feedback regulation between proteins. Notably, even though the protein-to-protein feedback regulation described above had been validated by previous biological experiments (*72-76, 82-91*), our claims focused primarily on establishing a dynamical logical connection between these isolated regulatory processes from a global perspective. For the purpose of validating this dynamic molecular mechanism, one may wonder why the (L_1, H_2) and (H_1, L_2) states did not appear in this scheme. We know from experimental evidence that the absence of the (L_1, H_2) and (H_1, L_2) states was due to the strong correlation between intra- and extra-nuclear fluorescence intensities. If the four fates emerge on the landscape of intra- and extra-nuclear fluorescence intensities of Fus3, the Pearson correlation coefficient between these two types of trajectories would be zero (*108*). Moreover, the feedback model of forward activation and negative inhibition favored the formation of two states from a physical standpoint **(Fig. 3D)**.

Between steady states, the cellular decision-making is primarily reflected by the transition rate, transition probability, residence time, and potential barrier height. Due to the relative nature of the high and low states at each pheromone concentration, their physical characteristics can be compared directly, but not at different concentrations. To compare the relative significance of these physical characteristics at different concentrations, a similar normalized approach (high/low) was used. At 0.7–0.8 μM, a slight increase in barrier height significantly lengthened the residence time of the high state. At 1.0–3.0 μM, the residence time also decreased gradually as the barrier height decreased **(Fig. 4D)**. In our biological system, the positive correlation statement regarding barrier height and residence time was confirmed **(Fig. 4C)**. Certainly, such physical characteristics that quantify cellular decision-making have significant biological implications for the study of yeast response behavior. Positive feedback regulation in the gene network ("Pheromone → Fus3" and "Fus3 → Fus3"), for example, increased the potential barrier height on the gene expression

landscape, whereas negative feedback regulation decreased it (I_1, I_2) **(Fig. 1 and Fig. 3C)**. The residence time at various pheromone concentrations revealed which gene expression fate yeast cells preferred in response to the pheromone.

Some studies believe that the establishment of polarity helps organisms to survive better in nature (*109, 110*). Due to the inability of yeast's chemotactic response to swim as that of E. coli, its polar growth could only grow in the direction of a high concentration of pheromone, achieving mutual contact and fusion between heterosexual yeasts (*2, 6, 111*). To quantify the mesoscopic behavior of yeast cells in polar growth, which grew and stopped intermittently, the yeast cells were characterized as a combination of filled circles. The white edge of the yeast cell image was the cell wall **(Fig. 5A).** Therefore, the cell filling circles were based on the outermost edge of the cell wall as the cell boundary. Rather than using the cell area, the total length, or the arithmetic mean of the length, we chose to describe the cell morphology using the reciprocal of the radius in the cell-filled circle multiplied by the number of filled circles, i.e., $H_n = n(\frac{1}{R_1} + \frac{1}{R_2} + \ldots + \frac{1}{R_n})$. This method has the following advantages: first, it could reflect the deformation of different parts of the cell; and second, H_n is a statistic that can reflect both the process and outcome of the cell polarity growth. It was important to note that when a cell grew laterally, its length also increased, so the terms lateral growth and longitudinal growth were relative rather than absolute descriptions of length and width.

The cell growth rate primarily characterized the process of cell polar growth, whereas the cell morphology primarily characterized the outcome. Specifically, the cell growth rate is actually the cell deformation rate. To verify the molecular mechanism of the growth rate for directional (model L) and non-directional (model W) growth, we constructed a dual fluorescence system (*CDC24*_GFP-*FUS3*_RFP) to demonstrate that there was a time lag in the multilevel protein signaling behavior. Due to the different maturation times of the two fluorescent proteins (GFP and RFP), the lag time between Fus3 and Cdc24 was only a relative quantity. Nonetheless, the delay time of the dual-fluorescence system at different positions was used to quantify the practical significance of multipolar signal transduction. Notably, the non-directional growth (model W: P_2) did not consist solely of the polar growth pathway of P_2, but rather a relative weight simplification to differentiate it from the directional growth (model L: P_1+P_2). To confirm that the fast growth rate (model F) and slow growth rate (model S) corresponded to the high and low states of Fus3, we explored the association between growth rates and dual fluorescent gene expression states. The high state (H_1, H_2) was primarily included in the fast growth rate, whereas the low state (L_1, L_2) was primarily included in the slow growth rate, confirming the molecular mechanism of F and S **(Fig. 5H and Table 3)**. In addition, there must be a lag between the expression of Fus3p and the observed cell growth, resulting in a low fluorescence state during fast cell growth and a high fluorescence state during slow cell growth.

For statistical analysis of different cell morphologies, we distinguished four cell morphological fates roughly as F_1-F_4 to provide a more intuitive description **(Fig. 6A)**. Nevertheless, the division of actual cell morphological fate was determined by fitting the trajectories, and not arbitrarily by the size of H_n. Given that H_n is extremely sensitive to changes in length and width in different parts of the cell, the area of cells that were morphologically divided into the four categories did not differ significantly from their overall appearance **(Fig. 6B)**. Our justification for proposing the molecular mechanisms of the four cell morphological fates is that morphology is the accumulation of a growth process. Due to the fact that the cell morphology described by H_n resembled the relative length and width of a cell, the capacity to grow in both directions can explain the emergence of cell morphologies **(Fig. 6C)**. In addition, in the statistical

graph of cell morphology, other fates tended to disappear, with the exception of the increase in the proportion of F_2. This indicated that the intracellular phase transition trend occurred at 3.0 μM as a result of enhanced negative feedback regulation (I_2 in **Fig. 1**). The coordinates of the cell morphology statistics chart at 3.0 μM were deviated from those of other concentrations due to the phase transition trend in the system, which altered the measurement scale of the four morphological fates. To explain the physics of the phase transitions in the biological system, we quantified the degree to which the detailed balance collapsed by employing the net flux characterizing the non-equilibrium statistical physics. The results demonstrated that the non-equilibrium dynamics of the biological system was supported by the significant increase in net flux of the morphological system at high pheromone dose (3.0 μM), causing the instability and phase transition.

Finally, we developed a simplified model of the gene regulatory network for signal transduction in order to confirm the global rationality of the dynamic sequential mechanism. Thus far, we have established the logical links between the functions of regulated proteins in the pheromone pathway for mating through the underlying signal transduction process. Despite the fact that our proposed validation method differs from the conventional validation method of constructing yeast mutants, it was capable of observing realistic cellular response behavior. Therefore, we will conduct dual-fluorescence systems in the future to reveal the dynamic relationship between signaling pathways, such as crosstalk.

455 **MATERIALS AND METHODS**

456 **Yeast strains and Growth media**

457 The yeast strain used in this experiment is *Saccharomyces cerevisiae* S288C (ATCC 201388:
458 *MAT*a*his*3Δ1 *leu*2Δ0 *met*15Δ0 *ura*3Δ0) (*112*). In the yeast fluorescence library, we choose a
459 special yeast as the research object, whose c-terminal of Fus3 is fused with GFP as the reporter
460 protein. The yeasts are cultured by inoculating 5ml of YNB [Yeast Nitrogen Base Without Amino
461 Acids (6.8 g/L), Dextrose (5 g/L), Uracil (76mg/L), 50×MEM Amino Acids (20ml/L)] medium
462 with a colony from a YPD agar plate [Yeast extract (10 g/L), Peptone (20 g/L), Dextrose (20 g/L),
463 Agar (10 g/L)]. Cells are grown overnight at 30℃ shaking at 250 rpm (about 14h). Before starting
464 the experiment, we take out 20ul of overnight cultures and dilute 100-fold in 2ml YNB medium to
465 obtain an optical density of 0.1 at 600 nm (OD600nm).

466 **Flow cytometry**

467 To determine the critical concentration of pheromone, we chose a flow cytometer for
468 preliminary screening. We set 8 different concentrations (0.01μM, 0.05μM, 0.1μM, 0.2 μM, 0.4μM,
469 0.6μM, 1.0μM, 1.5μM) for the pheromone medium, and culture the yeast cells in a shaker at 250
470 rpm and 30℃. In order to avoid contamination of the yeast cells, we have set up 5 sets of parallel
471 culture samples for each concentration of the medium. After culturing on a shaker for specific
472 times (3h, 6h, 9h, 12h and 24h), 105,000 cells are taken from each sample for analysis using the
473 flow cytometer.

474 **Microfluidic system platform**

475 We use the 4-chamber cell culture plate, CellASIC™ ONIX Y04C-02 Microfluidic Plate, for
476 live cell culture at 30°C. The plate is designed for use with the CellASIC™ ONIX Microfluidic
477 System, which provides a controlled dynamical microenvironment for cells. First, the yeast cells
478 are cultured in a microfluidic plate containing conventional YNB medium for 1 hour to adapt to
479 the new environment, and then switch to YNB medium supplemented with pheromone and culture
480 at a flow rate of 1 psi for 30 hours.

481 **Microscopy Measurements**

482 The fluorescence values of the single cells were measured using an inverted fluorescence
483 microscopy (Ti-E, Nikon) with automated stage and focus, equipped with a high NA oil-immersion
484 objective (1.45NA, 100×). We applied 488nm laser and set the output power at 30mW (only 10%
485 of the laser beam into the microscope objective), the fluorescence signals were collected by a
486 cooled EM-CCD camera (897U, Andor). All images were acquired using both bright field imaging
487 and fluorescent field imaging. These images were acquired by Nikon software. Data analysis were
488 accomplished through a combination of manual and automated analysis using custom Matlab code.
489 Many trajectories were taken from a time-lapse microscopy. The fluorescent images were
490 periodically captured and recorded every 10 minutes. The fluorescent data of each cell at each time
491 point were collected for the following discussion.
492

References and Notes:

1. H. C. Berg, D. A. Brown, Chemotaxis in Escherichia coli analysed by three-dimensional tracking. *Nature***239**, 500-504 (1972).
2. R. M. Macnab, D. E. Koshland, The gradient-sensing mechanism in bacterial chemotaxis. *Proceedings of the National Academy of Sciences***69**, 2509-2512 (1972).
3. D. Kedrin, J. van Rheenen, L. Hernandez, J. Condeelis, J. E. Segall, Cell motility and cytoskeletal regulation in invasion and metastasis. *Journal of mammary gland biology and neoplasia***12**, 143-152 (2007).
4. N. Vladimirov, V. Sourjik, Chemotaxis: how bacteria use memory. (2009).
5. J. Yuan, K. A. Fahrner, L. Turner, H. C. Berg, Asymmetry in the clockwise and counterclockwise rotation of the bacterial flagellar motor. *Proceedings of the National Academy of Sciences***107**, 12846-12849 (2010).
6. V. Sourjik, N. S. Wingreen, Responding to chemical gradients: bacterial chemotaxis. *Current opinion in cell biology***24**, 262-268 (2012).
7. H. Levine, W.-J. Rappel, The physics of eukaryotic chemotaxis. *Physics today***66**, (2013).
8. S. De Oliveira, E. E. Rosowski, A. Huttenlocher, Neutrophil migration in infection and wound repair: going forward in reverse. *Nature Reviews Immunology***16**, 378 (2016).
9. F. Xu, R. Bierman, F. Healy, H. Nguyen, A multi-scale model of Escherichia coli chemotaxis from intracellular signaling pathway to motility and nutrient uptake in nutrient gradient and isotropic fluid environments. *Computers & Mathematics with Applications***71**, 2466-2478 (2016).
10. L. Kőhidai, Chemotaxis: the proper physiological response to evaluate phylogeny of signal molecules. *Acta Biologica Hungarica***50**, 375-394 (1999).
11. P. J. Zhou *et al.*, Stochasticity Triggers Activation of the S-phase Checkpoint Pathway in Budding Yeast. *Physical Review X***11**, (2021).
12. J. E. Slessareva, H. G. Dohlman, G protein signaling in yeast: new components, new connections, new compartments. *Science***314**, 1412-1413 (2006).
13. R. E. Chen, J. Thorner, Function and regulation in MAPK signaling pathways: Lessons learned from the yeast Saccharomyces cerevisiae. *Bba-Mol Cell Res***1773**, 1311-1340 (2007).
14. Y. Q. Wang, H. G. Dohlman, Pheromone signaling mechanisms in yeast: A prototypical sex machine. *Science***306**, 1508-1509 (2004).
15. M. C. Gustin, J. Albertyn, M. Alexander, K. Davenport, MAP Kinase Pathways in the YeastSaccharomyces cerevisiae. *Microbiology and Molecular biology reviews***62**, 1264-1300 (1998).
16. I. Herskowitz, Life cycle of the budding yeast Saccharomyces cerevisiae. *Microbiological reviews***52**, 536 (1988).
17. C. M. Hull, R. M. Raisner, A. D. Johnson, Evidence for mating of the" asexual" yeast Candida albicans in a mammalian host. *Science***289**, 307-310 (2000).
18. J. Warringer *et al.*, Trait variation in yeast is defined by population history. *PLoS Genet***7**, e1002111 (2011).
19. E. Zörgö *et al.*, Ancient evolutionary trade-offs between yeast ploidy states. *PLoS Genet***9**, e1003388 (2013).
20. D. Norris, M. Osley, The two gene pairs encoding H2A and H2B play different roles in the Saccharomyces cerevisiae life cycle. *Molecular and Cellular Biology***7**, 3473-3481 (1987).
21. J. E. Haber, Mating-type genes and MAT switching in Saccharomyces cerevisiae.

*Genetics***191**, 33-64 (2012).
22. M. Z. Bao, M. A. Schwartz, G. T. Cantin, J. R. Yates III, H. D. Madhani, Pheromone-dependent destruction of the Tec1 transcription factor is required for MAP kinase signaling specificity in yeast. *Cell***119**, 991-1000 (2004).
23. D. D. Jenness, A. C. Burkholder, L. H. Hartwell, Binding of α-factor pheromone to yeast a cells: chemical and genetic evidence for an α-factor receptor. *Cell***35**, 521-529 (1983).
24. H. Youk, W. A. Lim, Secreting and sensing the same molecule allows cells to achieve versatile social behaviors. *Science***343**, 1242782 (2014).
25. H. Youk, W. A. Lim, Secreting and Sensing the Same Molecule Allows Cells to Achieve Versatile Social Behaviors. *Science***343**, 628-+ (2014).
26. M. D. Rose, Nuclear fusion in the yeast Saccharomyces cerevisiae. *Annu Rev Cell Dev Bi***12**, 663-695 (1996).
27. L. Marsh, M. Rose, The pathway of cell and nuclear fusion during mating in S. cerevisiae. *COLD SPRING HARBOR MONOGRAPH SERIES***21**, 827-888 (1997).
28. J. M. White, M. D. Rose, Yeast mating: getting close to membrane merger. *Current biology***11**, R16-R20 (2001).
29. L. Bardwell, A walk-through of the yeast mating pheromone response pathway (vol 25, pg 1465, 2004). *Peptides***26**, 337-+ (2005).
30. J. N. Molk, K. Bloom, Microtubule dynamics in the budding yeast mating pathway. *Journal of cell science***119**, 3485-3490 (2006).
31. H. G. Dohlman, J. W. Thorner, Regulation of G protein-initiated signal transduction in yeast: Paradigms and principles. *Annu Rev Biochem***70**, 703-754 (2001).
32. A. M. Neiman, I. Herskowitz, Reconstitution of a Yeast Protein-Kinase Cascade in-Vitro - Activation of the Yeast Mek Homolog Ste7 by Ste11. *P Natl Acad Sci USA***91**, 3398-3402 (1994).
33. B. Errede, A. Gartner, Z. Zhou, K. Nasmyth, G. Ammerer, MAP kinase-related FUS3 from S. cerevisiae is activated by STE7 in vitro. *Nature***362**, 261-264 (1993).
34. P. M. P. Anne-Christine Butty, Linda S. Huang, Ira Herskowitz, Matthias Peter*, The Role of Far1p in Linking the Heterotrimeric G Protein to Polarity Establishment Proteins During Yeast Mating. *SCIENCE*, (1998).
35. D. Matheos, M. Metodiev, E. Muller, D. Stone, M. D. Rose, Pheromone-induced polarization is dependent on the Fus3p MAPK acting through the formin Bni1p. *The Journal of cell biology***165**, 99-109 (2004).
36. M. Peter, A. Gartner, J. Horecka, G. Ammerer, I. Herskowitz, FAR1 links the signal transduction pathway to the cell cycle machinery in yeast. *Cell***73**, 747-760 (1993).
37. E. Elion, B. Satterberg, J. Kranz, FUS3 phosphorylates multiple components of the mating signal transduction cascade: evidence for STE12 and FAR1. *Molecular biology of the cell***4**, 495-510 (1993).
38. R. L. Roberts, G. R. Fink, Elements of a single MAP kinase cascade in Saccharomyces cerevisiae mediate two developmental programs in the same cell type: mating and invasive growth. *Genes & development***8**, 2974-2985 (1994).
39. I. Herskowitz, MAP kinase pathways in yeast: for mating and more. *Cell***80**, 187-197 (1995).
40. E. A. Elion, J. A. Brill, G. R. Fink, FUS3 represses CLN1 and CLN2 and in concert with KSS1 promotes signal transduction. *Proceedings of the National Academy of Sciences***88**, 9392-9396 (1991).

41. E. Blackwell *et al.*, Effect of the pheromone-responsive Gα and phosphatase proteins of Saccharomyces cerevisiae on the subcellular localization of the Fus3 mitogen-activated protein kinase. *Molecular and cellular biology***23**, 1135-1150 (2003).
42. F. van Drogen, V. M. Stucke, G. Jorritsma, M. Peter, MAP kinase dynamics in response to pheromones in budding yeast. *Nature cell biology***3**, 1051-1059 (2001).
43. F. Chang, I. Herskowitz, Identification of a gene necessary for cell cycle arrest by a negative growth factor of yeast: FAR1 is an inhibitor of a G1 cyclin, CLN2. *Cell***63**, 999-1011 (1990).
44. Y. Shimada, M.-P. Gulli, M. Peter, Nuclear sequestration of the exchange factor Cdc24 by Far1 regulates cell polarity during yeast mating. *Nature cell biology***2**, 117-124 (2000).
45. J. E. Segall, Polarization of yeast cells in spatial gradients of alpha mating factor. *Proceedings of the National Academy of Sciences***90**, 8332-8336 (1993).
46. X. N. Fang *et al.*, Cell fate potentials and switching kinetics uncovered in a classic bistable genetic switch. *Nature Communications***9**, (2018).
47. Z. L. Jiang *et al.*, The emergence of the two cell fates and their associated switching for a negative auto-regulating gene. *Bmc Biology***17**, (2019).
48. P. A. Takizawa, A. Sil, J. R. Swedlow, I. Herskowitz, R. D. Vale, Actin-dependent localization of an RNA encoding a cell-fate determinant in yeast. *Nature***389**, 90-93 (1997).
49. A. Colman-Lerner *et al.*, Regulated cell-to-cell variation in a cell-fate decision system. *Nature***437**, 699-706 (2005).
50. R. M. Gordley *et al.*, Engineering dynamical control of cell fate switching using synthetic phospho-regulons. *P Natl Acad Sci USA***113**, 13528-13533 (2016).
51. Z. Jiang *et al.*, The emergence of the two cell fates and their associated switching for a negative auto-regulating gene. *BMC biology***17**, 1-14 (2019).
52. L. Zeng *et al.*, Decision making at a subcellular level determines the outcome of bacteriophage infection. *Cell***141**, 682-691 (2010).
53. A. Colman-Lerner *et al.*, Regulated cell-to-cell variation in a cell-fate decision system. *Nature***437**, 699-706 (2005).
54. X. Fang *et al.*, Cell fate potentials and switching kinetics uncovered in a classic bistable genetic switch. *Nature communications***9**, 1-9 (2018).
55. F. St-Pierre, D. Endy, Determination of cell fate selection during phage lambda infection. *Proceedings of the National Academy of Sciences***105**, 20705-20710 (2008).
56. N. Yosef, A. Regev, Impulse control: temporal dynamics in gene transcription. *Cell***144**, 886-896 (2011).
57. Z. Bar-Joseph, A. Gitter, I. Simon, Studying and modelling dynamic biological processes using time-series gene expression data. *Nature Reviews Genetics***13**, 552-564 (2012).
58. M. Behar, N. Hao, H. G. Dohlman, T. C. Elston, Dose-to-Duration Encoding and Signaling beyond Saturation in Intracellular Signaling Networks. *Plos Computational Biology***4**, (2008).
59. A. Doncic *et al.*, Compartmentalization of a Bistable Switch Enables Memory to Cross a Feedback-Driven Transition. *Cell***160**, 1182-1195 (2015).
60. J. Hasty, D. McMillen, F. Isaacs, J. J. Collins, Computational studies of gene regulatory networks: in numero molecular biology. *Nature Reviews Genetics***2**, 268-279 (2001).
61. H. Feng, J. Wang, Potential and flux decomposition for dynamical systems and non-equilibrium thermodynamics: Curvature, gauge field, and generalized fluctuation-dissipation theorem. *The Journal of chemical physics***135**, 234511 (2011).

62. C. Li, J. Wang, Landscape and flux reveal a new global view and physical quantification of mammalian cell cycle. *Proceedings of the National Academy of Sciences***111**, 14130-14135 (2014).
63. G. Balázsi, A. van Oudenaarden, J. J. Collins, Cellular decision making and biological noise: from microbes to mammals. *Cell***144**, 910-925 (2011).
64. J. Wang, K. Zhang, L. Xu, E. Wang, Quantifying the Waddington landscape and biological paths for development and differentiation. *Proceedings of the National Academy of Sciences***108**, 8257-8262 (2011).
65. J. Wang, K. Zhang, E. Wang, Kinetic paths, time scale, and underlying landscapes: A path integral framework to study global natures of nonequilibrium systems and networks. *The Journal of chemical physics***133**, 09B613 (2010).
66. J. Wang, C. Li, E. Wang, Potential and flux landscapes quantify the stability and robustness of budding yeast cell cycle network. *Proceedings of the National Academy of Sciences***107**, 8195-8200 (2010).
67. J. Wang, K. Zhang, E. Wang, Robustness and dissipation of mitogen-activated protein kinases signal transduction network: Underlying funneled landscape against stochastic fluctuations. *The Journal of chemical physics***129**, 10B602 (2008).
68. J. Wang, L. Xu, E. Wang, Potential landscape and flux framework of nonequilibrium networks: robustness, dissipation, and coherence of biochemical oscillations. *Proceedings of the National Academy of Sciences***105**, 12271-12276 (2008).
69. E. H. Davidson, D. H. Erwin, Gene regulatory networks and the evolution of animal body plans. *Science***311**, 796-800 (2006).
70. N. G. Van Kampen, *Stochastic processes in physics and chemistry*. (Elsevier, 1992), vol. 1.
71. W. Zheng, H. Zhao, E. Mancera, L. M. Steinmetz, M. Snyder, Genetic analysis of variation in transcription factor binding in yeast. *Nature***464**, 1187-1191 (2010).
72. A. Anders, B. Ghosh, T. Glatter, V. Sourjik, Design of a MAPK signalling cascade balances energetic cost versus accuracy of information transmission. *Nature communications***11**, 1-10 (2020).
73. H. G. Dohlman, J. Song, D. Ma, W. E. Courchesne, J. Thorner, Sst2, a negative regulator of pheromone signaling in the yeast Saccharomyces cerevisiae: expression, localization, and genetic interaction and physical association with Gpa1 (the G-protein alpha subunit). *Molecular and cellular biology***16**, 5194-5209 (1996).
74. M. Sugiyama, Y. Kaneko, S. Harashima, Yeast protein phosphatases Ptp2p and Msg5p are involved in G1–S transition, CLN2 transcription, and vacuole morphogenesis. *Archives of microbiology***191**, 721-733 (2009).
75. W. A. Laviña, M. Sugiyama, Y. Kaneko, S. Harashima, Identification of protein kinase disruptions as suppressors of the calcium sensitivity of S. cerevisiae Δ ptp2 Δ msg5 protein phosphatase double disruptant. *Archives of microbiology***192**, 157-165 (2010).
76. W. A. Laviña, M. Sugiyama, Y. Kaneko, S. Harashima, Functionally redundant protein phosphatase genes PTP2 and MSG5 co-regulate the calcium signaling pathway in Saccharomyces cerevisiae upon exposure to high extracellular calcium concentration. *Journal of bioscience and bioengineering***115**, 138-146 (2013).
77. A.-C. Butty, P. M. Pryciak, L. S. Huang, I. Herskowitz, M. Peter, The role of Far1p in linking the heterotrimeric G protein to polarity establishment proteins during yeast mating. *Science***282**, 1511-1516 (1998).

677 78. A. Nern, R. A. Arkowitz, A Cdc24p-Far1p-Gβγ protein complex required for yeast
678 orientation during mating. *The Journal of cell biology* **144**, 1187-1202 (1999).
679 79. A. Nern, R. A. Arkowitz, Nucleocytoplasmic shuttling of the Cdc42p exchange factor
680 Cdc24p. *The Journal of cell biology* **148**, 1115-1122 (2000).
681 80. A. Nern, R. A. Arkowitz, A Cdc24p-Far1p-Gbetagamma protein complex required for
682 yeast orientation during mating. *J Cell Biol* **144**, 1187-1202 (1999).
683 81. E. H. Chen, *Cell fusion: overviews and methods*. (Springer, 2008).
684 82. E. Szczurek, I. Gat-Viks, J. Tiuryn, M. Vingron, Elucidating regulatory mechanisms
685 downstream of a signaling pathway using informative experiments. *Molecular Systems*
686 *Biology* **5**, 287 (2009).
687 83. C. I. Maeder *et al.*, Spatial regulation of Fus3 MAP kinase activity through a reaction-
688 diffusion mechanism in yeast pheromone signalling. *Nature cell biology* **9**, 1319-1326
689 (2007).
690 84. A. Serrano *et al.*, Spatio-temporal MAPK dynamics mediate cell behavior coordination
691 during fungal somatic cell fusion. *Journal of cell science* **131**, (2018).
692 85. J. E. Kranz, B. Satterberg, E. A. Elion, The MAP kinase Fus3 associates with and
693 phosphorylates the upstream signaling component Ste5. *Genes & Development* **8**, 313-327
694 (1994).
695 86. M. J. Winters, R. E. Lamson, H. Nakanishi, A. M. Neiman, P. M. Pryciak, A membrane
696 binding domain in the Ste5 scaffold synergizes with Gβγ binding to control localization
697 and signaling in pheromone response. *Molecular cell* **20**, 21-32 (2005).
698 87. R. P. Bhattacharyya *et al.*, The Ste5 scaffold allosterically modulates signaling output of
699 the yeast mating pathway. *Science* **311**, 822-826 (2006).
700 88. M. K. Malleshaiah, V. Shahrezaei, P. S. Swain, S. W. Michnick, The scaffold protein Ste5
701 directly controls a switch-like mating decision in yeast. *Nature* **465**, 101-105 (2010).
702 89. T. Chen, J. Kurjan, Saccharomyces cerevisiae Mpt5p interacts with Sst2p and plays roles
703 in pheromone sensitivity and recovery from pheromone arrest. *Molecular and Cellular*
704 *Biology* **17**, 3429-3439 (1997).
705 90. T. R. Garrison *et al.*, Feedback phosphorylation of an RGS protein by MAP kinase in yeast.
706 *Journal of Biological Chemistry* **274**, 36387-36391 (1999).
707 91. S. C. Parnell *et al.*, Phosphorylation of the RGS protein Sst2 by the MAP kinase Fus3 and
708 use of Sst2 as a model to analyze determinants of substrate sequence specificity.
709 *Biochemistry* **44**, 8159-8166 (2005).
710 92. R. E. Chen, J. Thorner, Function and regulation in MAPK signaling pathways: lessons
711 learned from the yeast Saccharomyces cerevisiae. *Biochimica et Biophysica Acta (BBA)-*
712 *Molecular Cell Research* **1773**, 1311-1340 (2007).
713 93. H.-O. Park, E. Bi, Central roles of small GTPases in the development of cell polarity in
714 yeast and beyond. *Microbiology and molecular biology reviews* **71**, 48-96 (2007).
715 94. J. B. Moseley, B. L. Goode, The yeast actin cytoskeleton: from cellular function to
716 biochemical mechanism. *Microbiology and Molecular Biology Reviews* **70**, 605-645 (2006).
717 95. A. Doncic, M. Falleur-Fettig, J. M. Skotheim, Distinct interactions select and maintain a
718 specific cell fate. *Molecular cell* **43**, 528-539 (2011).
719 96. N. Barkai, M. D. Rose, N. S. Wingreen, Protease helps yeast find mating partners.
720 *Nature* **396**, 422-423 (1998).
721 97. B. D. Slaughter, J. W. Schwartz, R. Li, Mapping dynamic protein interactions in MAP
722 kinase signaling using live-cell fluorescence fluctuation spectroscopy and imaging.

Proceedings of the National Academy of Sciences **104**, 20320-20325 (2007).
98. E. A. Elion, M. Qi, W. Chen, Signaling specificity in yeast. *Science* **307**, 687-688 (2005).
99. D. Fiedler *et al.*, Functional organization of the S. cerevisiae phosphorylation network. *Cell* **136**, 952-963 (2009).
100. J. Wang, Landscape and flux theory of non-equilibrium dynamical systems with application to biology. *Advances in Physics* **64**, 1-137 (2015).
101. X. Fang, K. Kruse, T. Lu, J. Wang, Nonequilibrium physics in biology. *Reviews of Modern Physics* **91**, 045004 (2019).
102. H. Feng, K. Zhang, J. Wang, Non-equilibrium transition state rate theory. *Chemical Science* **5**, 3761-3769 (2014).
103. X. N. Fang, K. Kruse, T. Lu, J. Wang, Nonequilibrium physics in biology. *Reviews of Modern Physics* **91**, (2019).
104. A. Nern, R. A. Arkowitz, G proteins mediate changes in cell shape by stabilizing the axis of polarity. *Molecular cell* **5**, 853-864 (2000).
105. D. T. Gillespie, The chemical Langevin equation. *The Journal of Chemical Physics* **113**, 297-306 (2000).
106. D. T. Gillespie, Approximate accelerated stochastic simulation of chemically reacting systems. *The Journal of chemical physics* **115**, 1716-1733 (2001).
107. H. De Jong, Modeling and simulation of genetic regulatory systems: a literature review. *Journal of computational biology* **9**, 67-103 (2002).
108. J. Lee Rodgers, W. A. Nicewander, Thirteen ways to look at the correlation coefficient. *The American Statistician* **42**, 59-66 (1988).
109. A. Treuner-Lange, L. Sogaard-Andersen, Regulation of cell polarity in bacteria. *J Cell Biol* **206**, 7-17 (2014).
110. J. Dworkin, Cellular Polarity in Prokaryotic Organisms. *Csh Perspect Biol* **1**, (2009).
111. L. Bardwell, A walk-through of the yeast mating pheromone response pathway. *Peptides* **25**, 1465-1476 (2004).
112. S. Ghaemmaghami *et al.*, Global analysis of protein expression in yeast. *Nature* **425**, 737-741 (2003).

Acknowledgments:

We acknowledge the support of the National Natural Science Foundation of China and the Changchun Institute of Applied Chemistry for this paper.

Funding:

SL was supported by the National Natural Science Foundation of China with Grant No.21721003.

Competing interests: Authors declare that they have no competing interests.

Data and materials availability: All data are available in the main text or the supplementary materials.

Figure Legends:

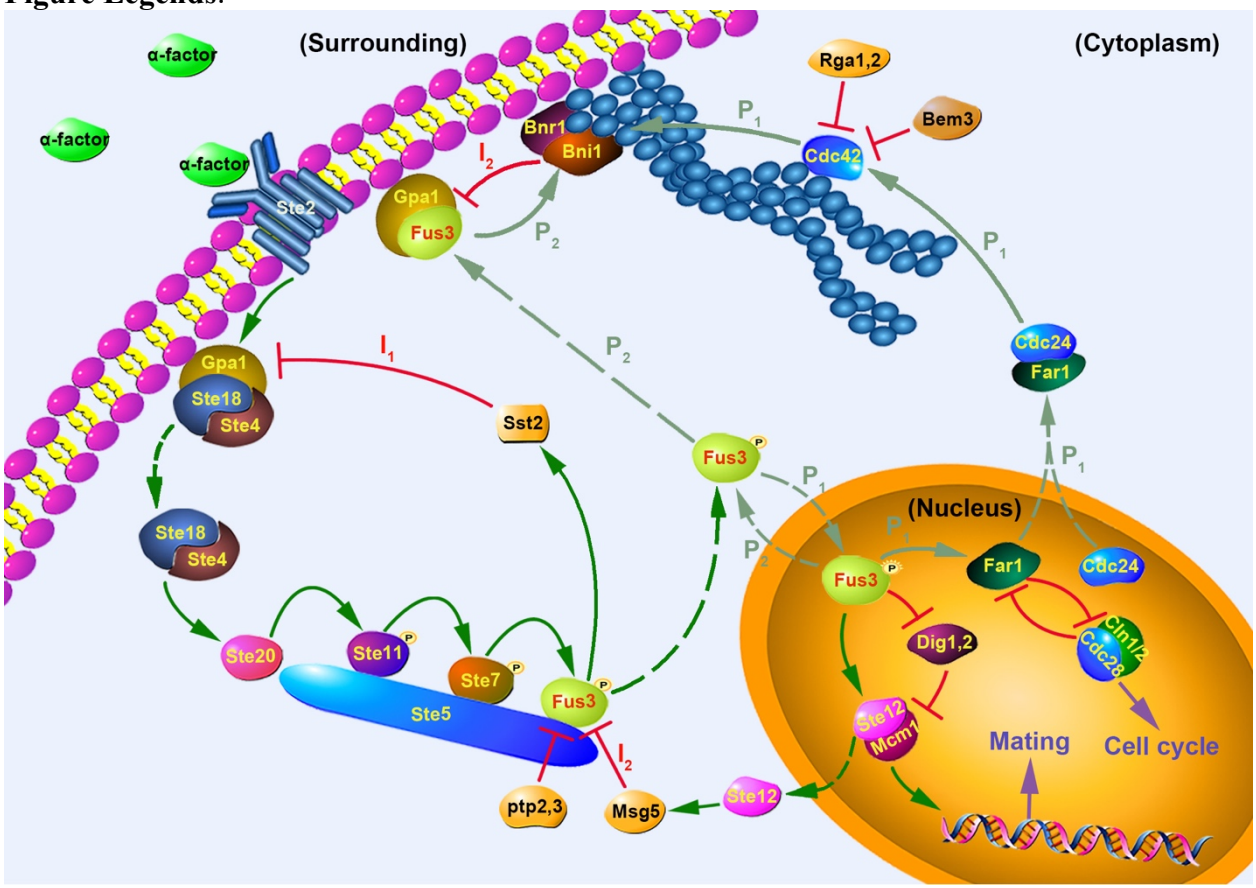

Fig. 1. Schematic diagram of the mating signal pathway of the yeast cell pheromone pathway. The red horizontal line represents the inhibition of negative feedback; the green arrow represents the activation of positive feedback; the dashed arrow represents a shift in localization; I_1 andI_2 represent different negative feedback adjustment pathways; and P_1 and P_2 represent the two polar growth signaling pathways that are connected by light green arrows.

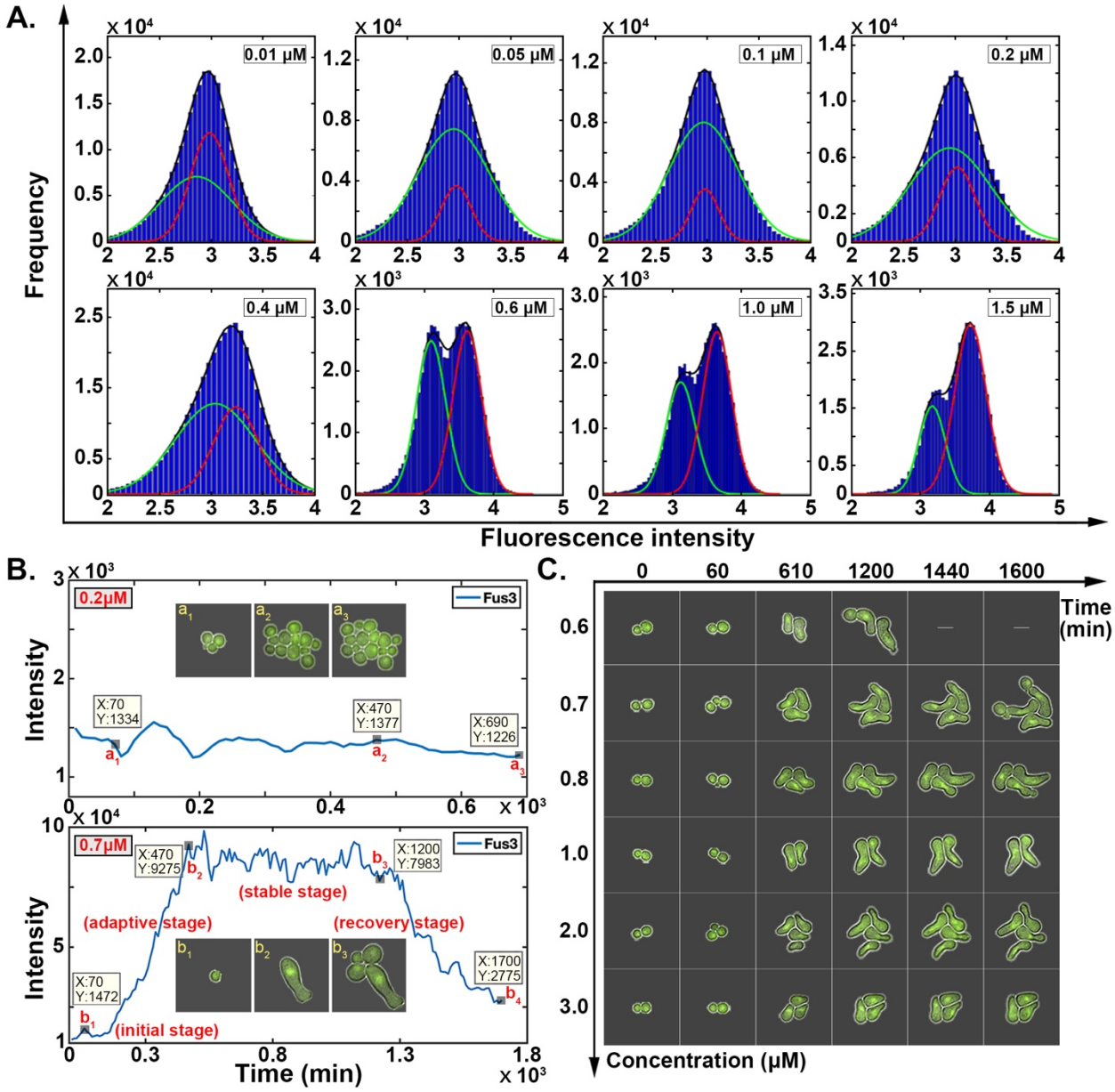

Fig. 2. A non-equilibrium biological model for cellular responses. (A) The fluorescence intensity of *FUS3*-GFP was measured using flow cytometry. The yeast cells were cultured in YPD medium containing different concentrations of pheromone for 24 h; the black curve represents the overall fluorescence intensity statistics; and the green and red curves represent the two fitted statistical peaks. The sample size for each pheromone concentration test was 105,000 yeast cells. **(B)** Fus3 gene expression was observed microscopically in response to 0.2 μM and 0.7 μM pheromone. The x-axis represents the duration of exposure to the pheromone-containing medium. The y-axis represents the fluorescence intensity of *FUS3*-GFP; and images a_1–a_3 and b_1–b_3 depict the living states of yeast cells as observed through a microscope at their corresponding times. **(C)** The microscopically captured living state of yeast at various pheromone concentrations. The green fluorescence in cells represents the expression of *FUS3*-GFP; 60 min on the x-axis represents the time when yeast cells were switched to a culture medium containing pheromone.

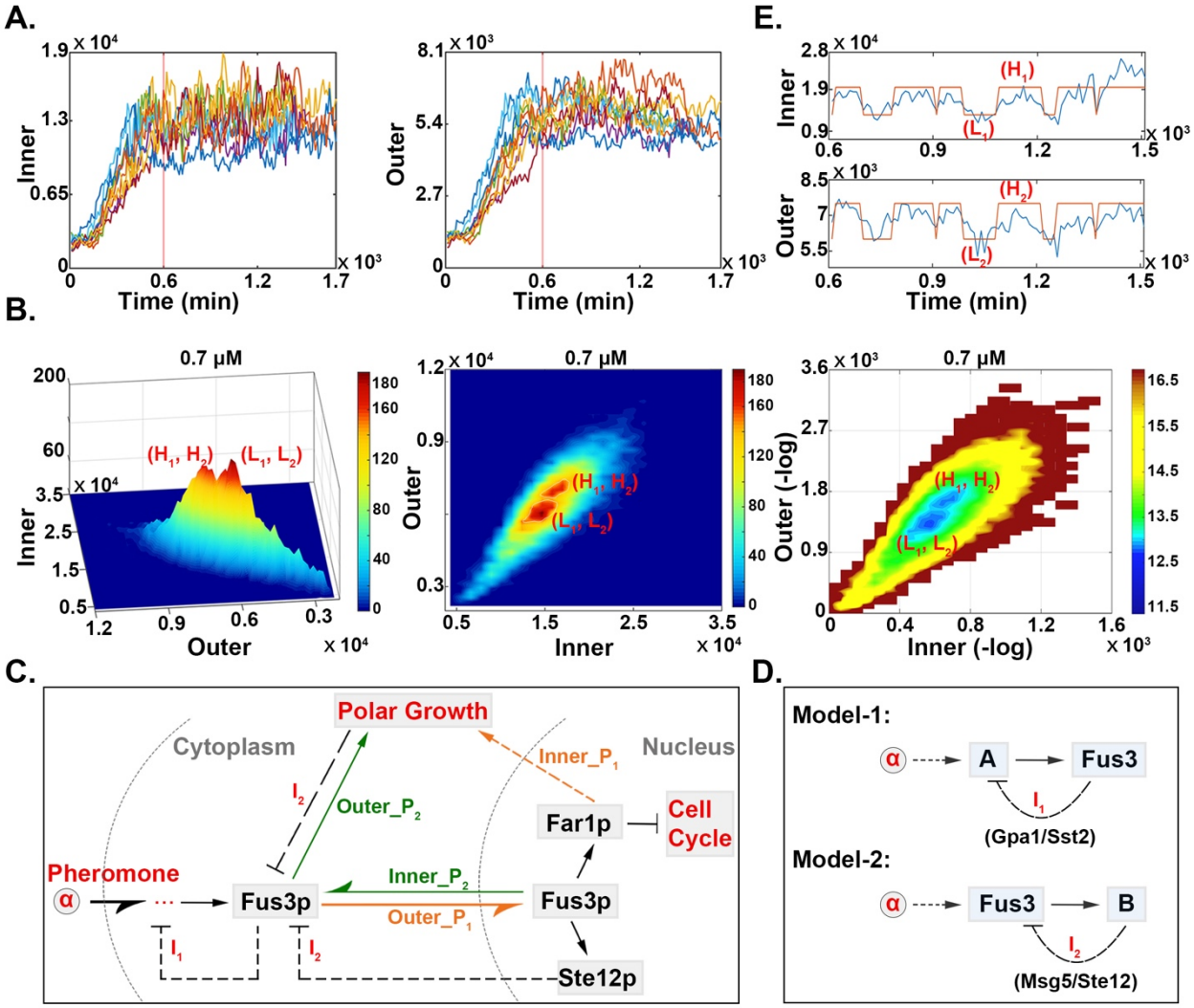

Fig. 3. The two steady states of expression levels of Fus3. (A) Trajectories of fluorescence intensity of Fus3 at 0.7 μM inside and outside the nucleus (only a portion shown). The red vertical line at 600 min was used to approximate the time node at which all cell fluorescence trajectories had entered a non-equilibrium steady state. **(B)** Three-dimensional distribution graph of Fus3 fluorescence intensity inside and outside the nucleus of yeast cells in the stationary phase under different pheromone concentrations. On the left is the 3D distribution of fluorescence or the 3D population landscape, in the middle is the 2D histograms or the 2D underlying potential landscapes U in exponential scale (defined as $p \sim e^{-U}$), which is also the population landscape; on the right is the 2D underlying potential landscapes U ($U = -\ln P$). The sample sizes at steady state for each pheromone concentration are as follows: 0.7 μM was equivalent to 21,335 cells, 0.8 μM to 18,408 cells, 1.0 μM to 23,041 cells, 2.0 μM to 36,886 cells, and 3.0 μM to 18,276 cells. **(C)** Diagram illustrating the molecular mechanism by which yeast cells respond to pheromone. The Outer_P_1 represents the indirect pathway taken by Fus3 from the cytoplasm to the nucleus in order to inhibit the cell cycle; Inner_P_1 represents the indirect pathway by which Fus3 in the nucleus promoted polar growth; Outer_P_2 represents the direct pathway of Fus3 in the cytoplasm for polar growth; Inner_P_2 represents the direct pathway for the transfer of Fus3 from the nucleus to the cytoplasm for polar growth; I_1 andI_2 represent the inhibitory effects of the negative feedback regulation; and the two gray dashed lines represent the cell membrane and the nuclear membrane. **(D)** Schematic

representation of two negative feedback models for regulating Fus3 gene expression. A and B represent, respectively, two different types of proteins that interact with Fus3 in the signaling pathway; "α" stands for α-factor pheromone. **(E)** The fluorescence intensity trajectories of Fus3 inside and outside the nucleus are over time. The red line represents the fitting line of the high state and the low state.

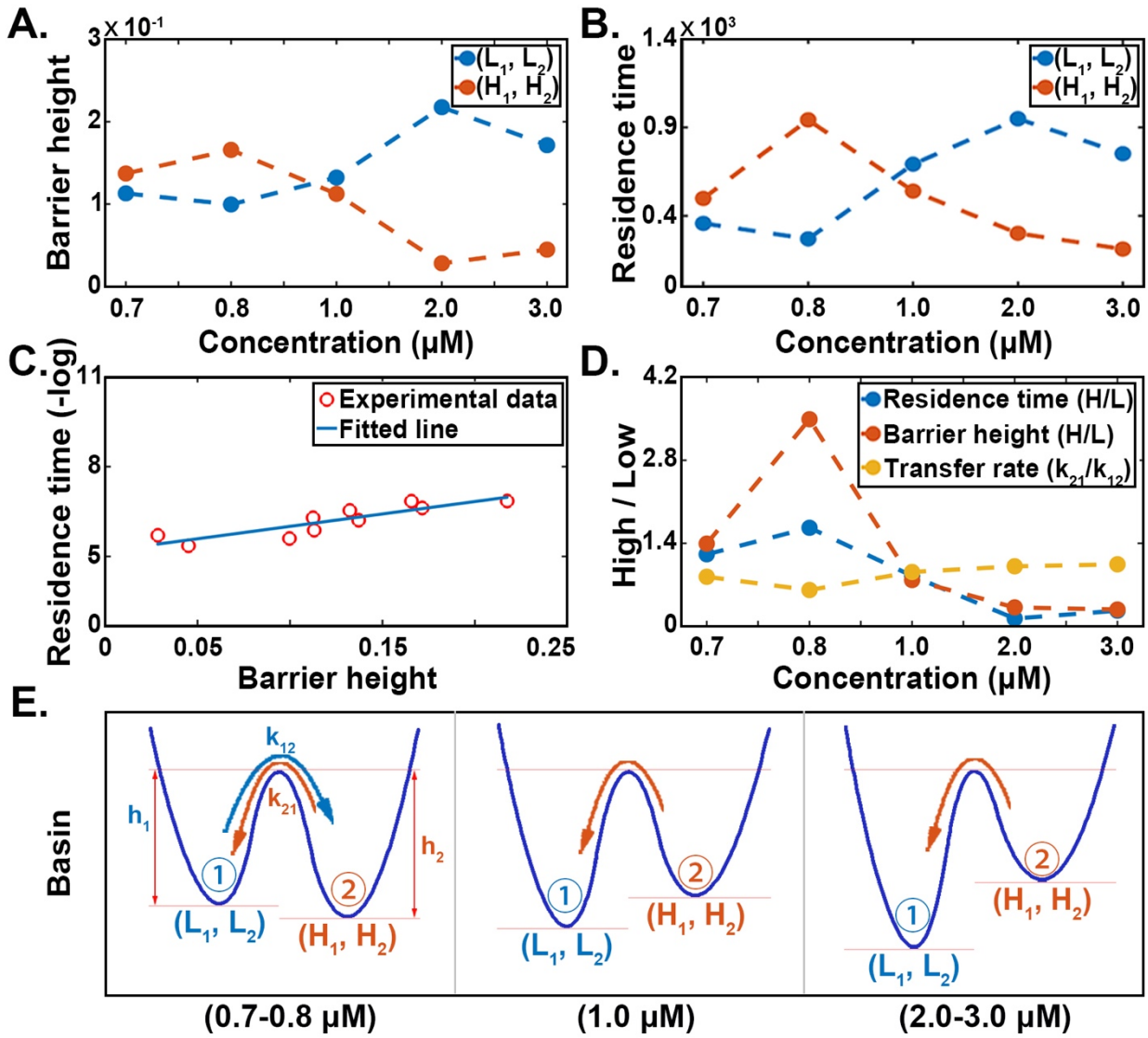

Fig. 4. The physical characteristics of cellular decision-making landscapes. (A) Trends in the statistical distribution of barrier heights for high and low states at varying pheromone concentrations. **(B)** Trends in the statistical distribution of residence time for high and low states at varying pheromone concentrations. **(C)** Correlation analysis between residence time and barrier height. The red circles are the data points; the blue line is the fitted line of the data. **(D)** The ratio of the physical characteristics of high and low states at various concentrations. The k_{12} is the transition rate from a low state to a high state; k_{21} is the transition rate from a high state to a low state. **(E)** Simple schematic diagram of the potential landscape topography under different pheromone dosages. ① stands for the low state, ② stands for the high state; k_{12} and k_{21} are the transition rates between the low state and the high state, respectively; h_1 and h_2 represent the respective barrier heights of the low and high states, respectively.

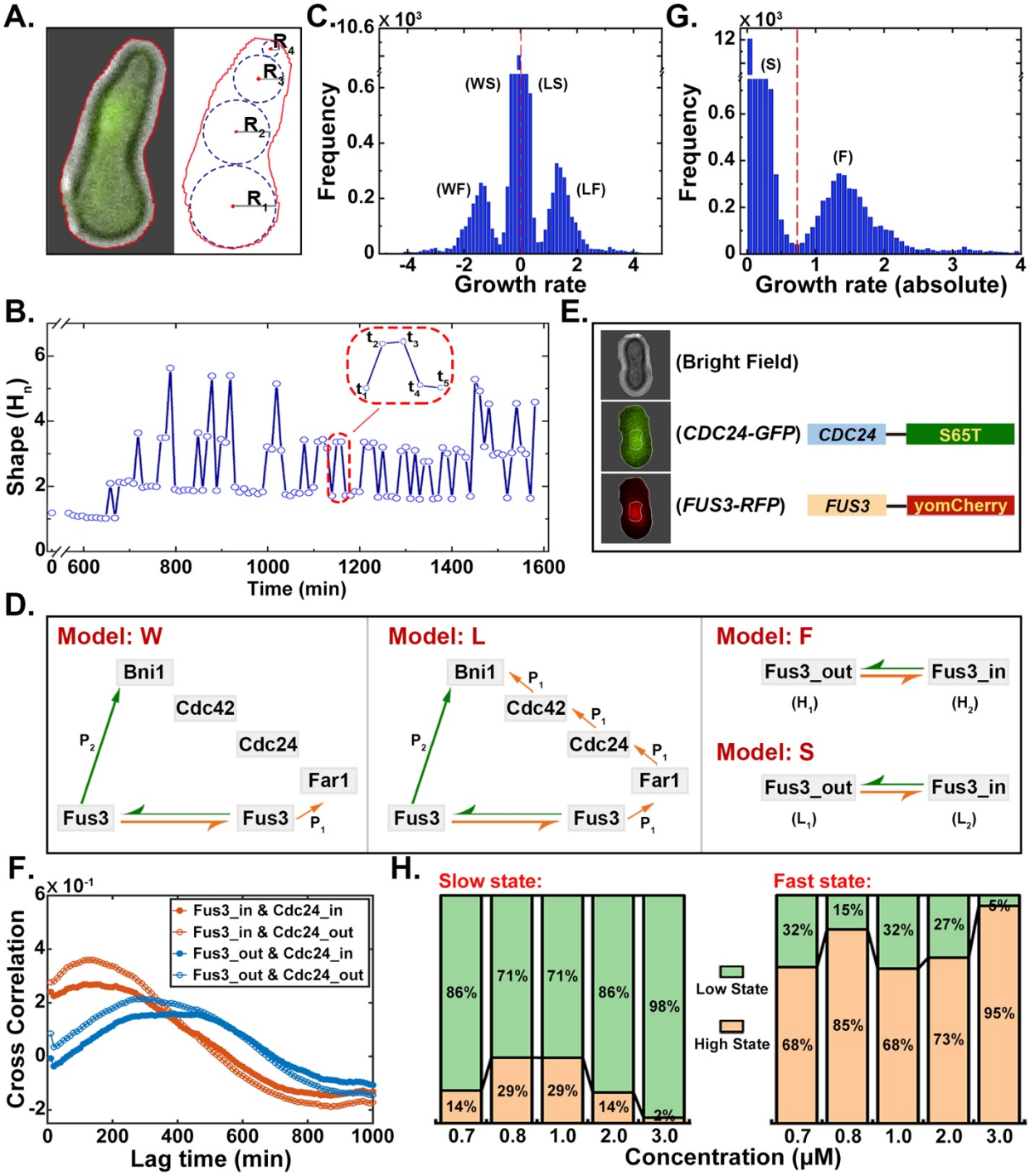

Fig. 5. Quantification of the deformation of yeast cells during polar growth. (A) A simple diagram of cell shapes with circle filling patterns. The image on the left depicts a yeast cell cultured for 1,020 min in a medium containing 0.7 μM pheromone; the red line indicates the contour of the cell; the image on the right is the filling model for the image on the left; $R_1 - R_4$ are the radii of the circle. **(B)** Real-time trajectory of the cell morphology (H_n) at 0.7 μM. **(C)** The distribution statistics of the cell growth rate at 0.7 μM. The red dashed line serves as the dividing line between positive and negative data. WF and LS represent the lateral-fast and lateral-slow rates, respectively; LF and WS represent the longitudinal-fast and longitudinal-slow rates, respectively. **(D)** Schematic

833 illustration of the molecular mechanism underlying the formation of the four growth rates. Model
834 W indicates that the polar growth pathway P_1 is not yet connected, so only the P_2 pathway operates;
835 Model L depicts the cooperative operation of polar growth pathways P_1 and P_2. Models F and S
836 describe the polar growth patterns of the two growth forces, which correspond to the high and low
837 states of Fus3, respectively. **(E)** Dual fluorescent protein system in yeast. The three images on the
838 left, from top to bottom, depict bright field cells, cells excited at 488 nm, and cells excited at 561
839 nm. The white circle within the cell represents the nucleus boundary; S65T and yomCherry are the
840 fluorescent proteins that were linked to *CDC24* and *FUS3*, respectively. **(F)** Cross-correlation of
841 two levels of gene expression at distinct positions. Gene_in and gene_out represent the gene
842 expression levels inside and outside the nucleus, respectively. **(G)** Statistical graph of the
843 distribution statistics of the absolute value of the cell growth rate at 0.7 μM. **(H)** The proportion
844 of high-state and low-state data present in high and low states at various pheromone concentrations.
845

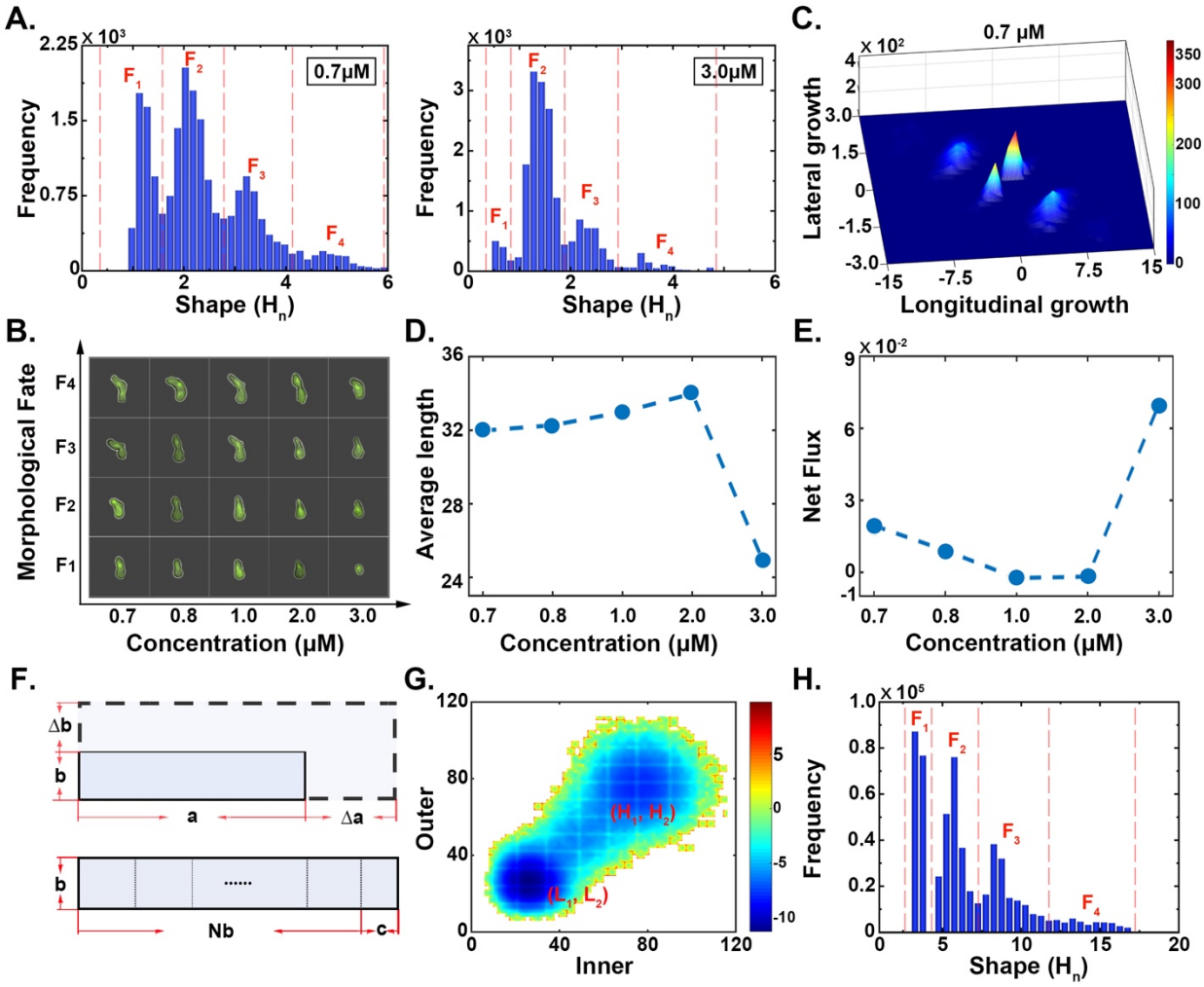

Fig. 6. The interpretation of the different cell morphological fates. (A) Statistical distribution of the cell morphology at 0.7 μM. The red dashed lines roughly correspond to the boundary between distinct cell morphological fates; F_1–F_4represent the four cell morphological fates. **(B)** Photographs taken with a fluorescence microscope of cells exhibiting four distinct morphological fates in response to varying pheromone concentrations. **(C)** The synergistic effect of both lateral and longitudinal cell growth capabilities at a pheromone concentration of 0.7 μM. The x-axis represents the ability of the cells to grow longitudinally, as indicated by the rate of change in the sum of the radii of the filled circles within the cells, i.e., $(R_1 + R_2 + \cdots + R_n)'$; the y-axis represents the ability of cells to grow laterally, as indicated by the rate of change in the average radius of the filled circles within the cells, i.e., $(\frac{R_1+R_2+\cdots+R_n}{n})'$. **(D)** Changes in the average cell length as a function of pheromone concentration. **(E)** The sum of the net fluxes among the four cell morphologies at various pheromone concentrations. **(F)** The scheme for the simulated cell growth; a represents the length of the cell; Δa is the increased length of the cell; b represents the width of the cell; and Δb is the increased width of the cell; the scheme of the H_n calculation; c is the remainder of the cell length divided by b; N represents the number of b. **(G)** Distribution graph of the negative log of the value of the Fus3 fluorescence intensity inside and outside the nucleus of yeast cells in the stationary phase using simulation. **(H)** The distribution of the cell morphology (H_n) using simulation.

Table 1. Correlation coefficients of fluorescence trajectories. The "Pearson Correlation Coefficient" between the intranuclear and extranuclear fluorescence intensity trajectories at various pheromone concentrations.

Pheromone doses (μM)	**0.7**	**0.8**	**1.0**	**2.0**	**3.0**
Correlation (inside & outside)	0.8321	0.8647	0.8446	0.7752	0.8879

Table 2. Physical characterization of gene expression landscapes. The transition probability, transition rate, residence time, and barrier height between the high and low states at various pheromone concentrations.

Pheromone doses (μM)		**0.7**	**0.8**	**1.0**	**2.0**	**3.0**
Transition probability $\boldsymbol{P} = \begin{pmatrix} \boldsymbol{P_{11}} & \boldsymbol{P_{12}} \\ \boldsymbol{P_{21}} & \boldsymbol{P_{22}} \end{pmatrix}$	$\boldsymbol{P_{11}}$	0.69	0.74	0.5369	0.5502	0.6143
	$\boldsymbol{P_{12}}$	0.31	0.26	0.4631	0.4498	0.3857
	$\boldsymbol{P_{21}}$	0.3711	0.4251	0.5053	0.445	0.3686
	$\boldsymbol{P_{22}}$	0.6289	0.6289	0.6289	0.6289	0.628
Transition rate	$\boldsymbol{k_{12}}$	0.0623	0.0717	0.1803	0.112	0.0687
	$\boldsymbol{k_{21}}$	0.052	0.0439	0.1652	0.1132	0.0718
Residence time (min)	**low**	357.43	270	691.5	947.98	750.74
	high	498.17	941.84	539.63	301.44	212.3
Barrier height	**low**	0.1131	0.0997	0.1323	0.2175	0.1716
	high	0.1371	0.1657	0.1125	0.0285	0.0451

Table 3. The proportional distribution of high state (H_1, H_2) and low state (L_1, L_2) in two growth rates. "FH " denotes the "High state" in the "Fast growth rate"; "FL " denotes the "Low state" in the "Fast growth rate"; "SH " denotes the "High state" in the "Slow growth rate"; "SL" denotes the "Low state" in the "Slow growth rate"; "$FH + FL$" and "$SH + SL$" represent fast and slow growth rate data volumes.

Pheromone doses (μM)	$\frac{FH}{(FH+FL)}$	$\frac{FL}{(FH+FL)}$	$(FH+FL)$	$\frac{SH}{(SH+SL)}$	$\frac{SL}{(SH+SL)}$	$(SH+SL)$
0.7	0.6847	0.3153	13888	0.1433	0.8567	7447
0.8	0.8500	0.1500	5027	0.2879	0.7121	13381
1.0	0.6782	0.3218	1157	0.2872	0.7128	21884
2.0	0.7266	0.2734	2249	0.1353	0.8647	34637
3.0	0.9530	0.0470	1679	0.0244	0.9756	16597

Table 4. The Average length of yeast cells at different pheromone doses.

Pheromone doses (μM)	**0.7**	**0.8**	**1.0**	**2.0**	**3.0**
Average length	31.98	32.27	32.99	33.99	25.01

Supplementary Materials for

Global quantitative understanding of nonequilibrium fate decision making in response to pheromone

Sheng Li [1,2], Qiong Liu [2]*, Erkang Wang [1,2], Jin Wang [3]*

Affiliations:

[1]College of Chemistry, Jilin University, Changchun, Jilin, 130012 P. R. China.

[2]State Key Laboratory of Electroanalytical Chemistry, Changchun Institute of Applied Chemistry, Chinese Academy of Sciences, Changchun, Jilin, 130022, China.

[3]Department of Chemistry and of Physics and astronomy, State University of New York at Stony Brook, Stony Brook, New York, 11794-3400, USA.

*Corresponding author. Email: liuqiong@ciac.ac.cn; jin.wang.1@stonybrook.edu.

This PDF file includes:

Materials and Methods
Figs. S1 to S13
Tables S1 to S9
References

Other Supplementary Materials for this manuscript include the following:

Movies S1 to S9

Materials and Methods

Pheromone environment

The stimulus source we chose is pheromone, an alpha factor peptide hormone, whose molecular weight is 1683.98 (GenScript). We weigh a certain amount of powdered pheromone and dissolve them in YPD and YNB liquid medium respectively to prepare 1000μM pheromone medium, and then gradually dilute it to the ideal concentration medium for microscopy experiments and other experiments.

At the beginning, in order to adapt to the microfluidic environment, the yeast cells are cultured in the YNB conventional medium for 60 minutes, and then are switched to the medium supplemented with pheromone for culture.

Dual fluorescence system construction

When designing the vector for the gene editing of *FUS3*, we consulted the sequence of the plasmid "pFA6a-link-yomCherry-CaURA3". This plasmid's core sequence ("yomCherry-CaURA3") was incorporated into the homologous recombination target fragment that we designed **(Fig. S10)**. The recombinant vector that we designed consists primarily of the left and right homology arms (F/R) of the gene *FUS3*, the flexible chain connecting *FUS3* and the fluorescent group (linker), the red fluorescent gene (yomCherry), and the screening gene (CaURA3). Among them, the "yomCherry" is a red fluorescent protein; the "CaURA3" is a protein that can compensate for the uracil deficiency-induced lethality of yeast.

First, 300bp were chosen as the left and right homologous long arms (F'/R') before and after the stop codon (TAG) of the *FUS3* gene. The homology arms **(**F/R**)** within the sequence interval of F'/R' can be obtained by performing PCR with these homologous long arm primers. Second, we selected a flexible chain (6aa [GS]x linker) as a structural buffer in order to fuse the red fluorescent reporter gene ("yomCherry") to the 3' end of gene *FUS3* without destroying the protein structure between the two groups. Finally, the vector containing "yomCherry-CaURA3" was introduced into yeast cells. Table S9 lists the gene sequences we used.

Real time image analysis

Bright-field images obtained by the total internal reflection microscope were segmented, aligned, and labeled using a custom Matlab routine. We segmented the cells according to bright field images to obtain the outlines of the individual cells, and assigned each cell accordingly. Then we can collect the trajectories of the generations by the assigned id when the cells grow and divide, and obtain cell lineages. All the cell boundaries of yeast were manually corrected. The cell nuclei were distinguished by contouring the fluorescence images. Fluorescence intensity is the average of all fluorescence intensity within the cell boundary.

The real-time trajectories were obtained by automatic tracking, based on the cell overlaps between the adjacent frames. All trajectories require manual correction.

Steady-state image analysis

In order to explore the underlying mechanism of the bimodality, we collected the real time fluorescence intensity trajectories **(Fig. 3A and Fig. S1–S2)**, which show that the yeast response is in a steady state after about 600min. This state means that the fluorescence intensity of the yeast inside and outside the nucleus does not increase or decrease significantly. The histograms of inner

and outer fluorescence intensity were obtained by the steady-state fluorescence trajectories **(Fig. 3B and Fig. S3–S5)**.

The shape characteristics of the yeast are described by the H_n in the yeast. The growth rate of the yeast is the numerical differentiation of the H_n. All the trajectories can be used to provide the quantitative analysis through Hidden Markov Chain Model (HMM). During the HMM fitting, the parameters of the fluorescence state were fixed. The distribution of high fluorescence state and low fluorescence state in two growth rates can be obtained by counting the state points on the trajectories.

Data Analysis of the Time-Lapse Experiments

The cell state can be distinguished from the trajectories using hidden Markov model (HMM). A maximum likelihood estimate of HMM parameters was performed globally on all the time traces separately. Multiple random initial parameters were used to start the iterative HMM analysis and ensure convergence to the global minimum. The Baum-Welch algorithm was used to re-estimate the parameters at the end of each iteration. Steady-state condition was enforced on the re-estimated parameters in each iteration. HMM can be directly applied to two-dimensional and high-dimensional data. Therefore, the inner and outer fluorescence data can be trained by the HMM, the results showed that the yeast fluorescence has bimodal distribution. The detailed results are shown in **Fig. 2**. The overlap ratio between the two states is obtained by integrating the overlapping part of the peak of the two states, which needs the results fitted by HMM. For each trajectory, the state can be determined by the HMM, and the state sequence is shown in **Fig. 3E**. The total residence time and the number of state changes can be obtained by counting the state points on the trajectories, and the average residence time is the quotient of the total residence time and the number of state changes.

Distinguishing the boundaries of the nucleus

When yeast cells are stimulated by pheromones, two responses occur: first, the cell cycle is arrested in the G1 phase, and second, mating-related genes are activated. To ensure both responses, large amounts of Fus3 are delivered to the nucleus, causing Fus3 to form fluorescent clusters in the nucleus (*1-9*). Previous articles have employed the fluorescent cluster region as the nucleus (*10-12*). When we observed cell budding and division under the microscope, the fluorescence clusters split in half, which corresponds to the separation of the daughter cell's nucleus from the mother cell's nucleus, indicating that it is feasible to use the fluorescence cluster as the nucleus. We use an algorithm similar to contour lines to divide each pixel in a cell into four distinct calculation levels. Then, the fluorescent spots at the same contour level are joined into closed regions. By comparing each level individually, it was determined that the outer edge of the highest level, which serves as the boundary between the nucleus and the cytoplasm, is best able to encompass intracellular fluorescent clusters **(Fig. S11).** Therefore, we propose that fluorescence above this threshold is localized within the nucleus, whereas fluorescence below this threshold is localized outside of the nucleus.

Filled circle model in cell shape

After identifying the boundary of the cell shape with "Matlab", we filled it in with circles along the cell's long axis in turns, with the area of the circle filled in each time being guaranteed to be the largest area of the remaining unfilled part. To ensure the accuracy of the cell morphology

(H_n) at various stages, we set a minimum circle diameter (5 pixels) to avoid significantly increasing the shape's internal gap.

Characterizing the deformation behavior of yeast cells

To quantify the behavior of yeast cells of which deformation rate did not vary uniformly over time, we characterized various cell components using a circular fill pattern **(Fig. 5A)**. The largest circle represents the initial main part of the cell, while the smallest circle represents the newly formed portion at the top of the cell. For example, there are two filled circles denoted by the letters R_0 and R_1 within the yeast cell. R_0 is the larger of the two circles, whereas R_1 is the smaller **(Fig. S12)**. If the filled circle R_1 of the cells grows uniformly in size from small to large (model-1: "$R_{1_1} \rightarrow R_{1_2} \rightarrow R_{1_3} \rightarrow R_{1_4}$"), then the ratios of the smallest circle to the largest circle in the cell will be uniformly distributed. If, on the other hand, the cell grows as in model-2 ("$R_{1_1} \rightarrow R_{1_2} \rightarrow R_{1_3} \rightarrow R_{1_3} \rightarrow R_{1_4}$") with the growth temporarily halted at R_{1_3}, then R_{1_3} will be observed repeatedly, increasing the probability of the R_{1_3}/R_0. When the size ratio of the smallest and largest circles was used as an observable value, we noticed that the statistical result was mostly around 0.27 at 0.7 μM **(Fig. S13)**. This clearly demonstrated that when the size ratio was 0.27, the cell was growing more slowly or was temporarily not growing, and thus there were more opportunities to observe this ratio distribution during cell polar growth. That is, the rate of deformation or the capacity for growth at various locations within a cell were not exactly identical.

To quantify the various cell deformations that occur during cell growth, we considered a value (H_n) comparable to the harmonic mean to characterize the cell morphology, i.e., $H_n = n(\frac{1}{R_1} + \frac{1}{R_2} + \ldots + \frac{1}{R_n})$. The significant advantage of H_n is that it is particularly sensitive to small morphological changes at various locations of the cell. For example, we set the radius of the filled circle in the cell as R_1, R_2, and R_3 in advance. If the cell grew longitudinally (in length), a new filled circle (R_4) was added to the cell; consequently, the value of H_n increased as the number of elements in parentheses increased from three to four. In contrast, as cells expanded laterally (in width), the values of H_n decreased regardless of whether the filled circle's radius increased.

Derivation of the transition rates

The master equation can be written as

$$\frac{d}{dt}\begin{pmatrix} P_1 \\ P_2 \end{pmatrix} = \begin{pmatrix} k_{11} & k_{12} \\ k_{21} & k_{22} \end{pmatrix}\begin{pmatrix} P_1 \\ P_2 \end{pmatrix} = \begin{pmatrix} -a & b \\ a & -b \end{pmatrix}\begin{pmatrix} P_1 \\ P_2 \end{pmatrix}.$$

Here P_1 and P_2 are the probabilities of the low expression state and high expression state, respectively, while k_{ij} (i, j=1, 2) is the transition rate from P_i to P_j. We can write down the solution as follows with the initial conditions $P_1(0) = 1$, $P_2(0) = 0$,

$$P_1(\mathrm{t}) = \frac{b + ae^{-(a+b)t}}{a+b};\ P_2(\mathrm{t}) = -\frac{a(-1+e^{-(a+b)t})}{a+b}.$$

Then the transition probability between the low expression state and the low expression state is $P_{11} = P_1(\delta t) = \frac{b+ae^{-(a+b)\delta t}}{a+b}$, where δt is the observational time window for each time, here $\delta t = 10\ min$. With the initial conditions $P_1(0) = 0$, $P_2(0) = 1$,

$$P_1(\mathrm{t}) = -\frac{\mathrm{b}(-1+e^{-(a+b)t})}{a+b};\ P_2(\mathrm{t}) = \frac{a+be^{-(a+b)t}}{a+b}.$$

Then the transition probability between the high expression state and the high expression state is $P_{22} = P_2(\delta t) = \frac{a+be^{-(a+b)\delta t}}{a+b}$, where δt is the observation time window for each time, here $\delta t = 10\ min$.

According to the HMM analysis, when the pheromone dose is 0.7 μM, the transition matrix is $P = \begin{pmatrix} P_{11} & P_{12} \\ P_{21} & P_{22} \end{pmatrix} = \begin{pmatrix} 0.6900 & 0.3100 \\ 0.3711 & 0.6289 \end{pmatrix}$. So we can get the transition rate as: a= 0.052017 (1/min), b= 0.062270 (1/min).

Decomposing of the flux in the cell morphology

The kinetics of the cell morphological can be modeled by a four-state Markov process. The transition probability (M_{ij}) can be calculated by counting the number of transitions in the state trajectories. Therefore, the master equation can be shown as follows:

$$\frac{dP_i}{dt} = \sum_j M_{ij} P_i \qquad \textbf{(Equation 1)}$$

Where P_i represents the probability of state i, and the transition probability M_{ij} represents the transition probability from state i to state j. For steady state, we set the left term of the master equation (1) to zero, then we obtain the steady state solution P_i^S, which is the long time limit. The steady state flux between state i and j can be defined as: $F_{ij} = -M_{ij}P_i^S + M_{ji}P_j^S$. If the steady state of the system is in equilibrium state, the flux between any two nodes in the system is zero, that is the detailed balance condition. For the general biological system, it does not necessarily satisfy the detailed balance condition ($F_{ij} \neq 0$), the system is in non-equilibrium steady state, there will be at least one net flux among states.

In order to study the non-equilibrium steady states, we can separate the dynamical process into two parts, one is the detailed balance part and the other is the detailed balance-breaking kinetic process. To describe the detailed balance breaking, we decompose the probability matrix. The component of the rate matrix MP can be decomposed into two parts, one being the symmetric matrix and the other cycle matrix, that is

$$MP = C + D \qquad \textbf{(Equation 2)}$$

Where D is the symmetric matrix $D_{ij} = \left(M_{ij}P_i^S + M_{ji}P_j^S\right)/2$, C is the asymmetric matrix $C_{ij} = \left(M_{ij}P_i^S - M_{ji}P_j^S\right)/2$. Since the system contains four states, the asymmetric flux is not unique and contains three net cycle fluxes. Meanwhile, in order to ensure the consistency of decomposition for various pheromone concentration systems, the given base sets of flux decomposition were selected. Here, the base sets we selected are "State$_1$ –State$_2$ –State$_3$ –State$_1$", "State$_1$ –State$_4$ –State$_3$ –State$_1$", "State$_2$ –State$_4$ –State$_3$ –State$_2$", the corresponding net fluxes are J_1, J_2 and J_3. The asymmetric matrix C can be rewritten as follows:

$$C = \begin{pmatrix} 0 & \frac{J_1}{2} & -\frac{J_2}{2} - \frac{J_1}{2} & \frac{J_2}{2} \\ -\frac{J_1}{2} & 0 & \frac{J_1}{2} - \frac{J_3}{2} & \frac{J_3}{2} \\ \frac{J_1}{2} + \frac{J_2}{2} & -\frac{J_1}{2} + \frac{J_3}{2} & 0 & -\frac{J_2}{2} - \frac{J_3}{2} \\ -\frac{J_2}{2} & -\frac{J_3}{2} & \frac{J_2}{2} + \frac{J_3}{2} & 0 \end{pmatrix}$$

The linear equations can be obtained by corresponding the numerical results of the above matrix C and the experimental statistics **(Table S1–S5)**. For example, three linearly independent parameters of $C_{1,4}, C_{1,3}, C_{2,3}$ are selected for the linear equations originated from the underlying master equations.

The linear equations (0.7 μM) are $\begin{pmatrix} C_{1,4} = \frac{J_2}{2} = 0.0036 \\ C_{1,3} = -\frac{J_2}{2} - \frac{J_1}{2} = -0.0067 \\ C_{2,3} = \frac{J_1}{2} - \frac{J_3}{2} = 0 \end{pmatrix}$. Then, solving these linear equations one can get the net flux values of the non-equilibrium system.

The comprehensive description of the biochemical reactions in stochastic simulations.

The biochemical reactions in our signal transduction model were derived from the preexisting gene regulatory network. These biochemical reactions include the processes of gene translation into the proteins, the phosphorylation of the proteins, the degradation of the proteins, the interaction between the proteins, and the transfer of the proteins within the nucleus and the cytoplasm of the cells. The following is an understanding of each chemical reaction **(Table S8)**:

Reaction 1 depicts a portion of the gene *FUS3* being translated into a cytoplasmic protein at a certain rate. Reaction 2 depicts the gene *FUS3* generated by the indirect pheromone induction in addition to the known gene regulation. Reaction 3 is the reverse reaction of the reaction 2. Reaction 4 depicts the process of the phosphorylation of the protein produced by the gene *FUS3* induced by the pheromones outside the cell nucleus. Reaction 5 represents the gene *FUS3* produced by the self-activation of the phosphorylated protein Fus3 outside the cell nucleus. Reaction 6 is the reverse reaction of the reaction 5. Reaction 7 represents the process of the phosphorylation of a protein generated outside of the nucleus by the self-activating gene *FUS3*. Reaction 8 represents the transport of the phosphorylated Fus3 from the outside of the nucleus to the inside of the nucleus. Reaction 9 is the reverse reaction of the reaction 8.

Reactions 10 and 11 represent the degradation of the phosphorylated Fus3 both outside and inside the nucleus. Reaction 12 represents the translation of the gene *STE12* into the phosphorylated protein Ste12. Reaction 13 represents the impact of the gene *STE12* on the nuclear protein Fus3. Reaction 14 is the reverse reaction of the reaction 13. Reaction 15 represents the activation of the gene *STE12* by the nuclear Fus3. Reaction 16 represents the process of the translation of the gene *MSG5* into the phosphorylated protein Msg5. Reaction 17 represents the interaction between the phosphorylated protein Ste12 and the gene *MSG5*. Reaction 18 is the reverse reaction of the reaction 17. Reaction 19 represents the process of the translation of the gene *MSG5*, which is activated by the phosphorylated protein Ste12.

Reaction 20 represents the interaction between the phosphorylated protein *MSG5* and the gene *FUS3*. Reaction 21 is the reverse reaction of the reaction 20. The reaction 22 represents the inhibition of the gene *FUS3* expression by the phosphorylated protein *MSG5*. Reactions 23 and 24 represent the degradation of the proteins Ste12 and Msg5, respectively. Reaction 25 represents the process of the phosphorylation of protein Far1 generated by the gene *FAR1*. Reaction 26 represents the interaction between the Fus3 in the nucleus and the gene *FAR1*. Reaction 27 is the reverse reaction of reaction the 26. Reaction 28 represents the process of the transcription of the gene

FAR1, regulated by the Fus3, into the protein. Reaction 29 represents the degradation of the protein Far1.

Reaction 30 represents the process of the gene *BNI1* generating the protein Bni1. Reaction 31 represents the interaction between the cytoplasmic Fus3 and the gene *BNI1*. Reaction 32 is the reverse reaction of the reaction 31. Reaction 33 represents the process of the indirect inhibition of the Fus3 expression outside of the nucleus by Bni1. Reaction 34 represents the interaction between the nuclear gene *BNI1* and the phosphorylated Far1. Reaction 35 is the reverse reaction of the reaction 34. Reaction 36 represents the process of the phosphorylated Far1-activated generation of the phosphorylated protein from the gene *BNI1*. Reaction 37 represents the interaction between the nuclear Fus3 and the gene *BNI1*. Reaction 38 is the reverse reaction of the reaction 37. Reaction 39 represents the process of the generation of phosphorylated protein from the gene *BNI1* activated by the phosphorylated Fus3 outside of the nucleus.

Reactions 40 and 41 denote the degradation of the phosphoproteins Bni1 both in the cytoplasmic and nuclear compartments.

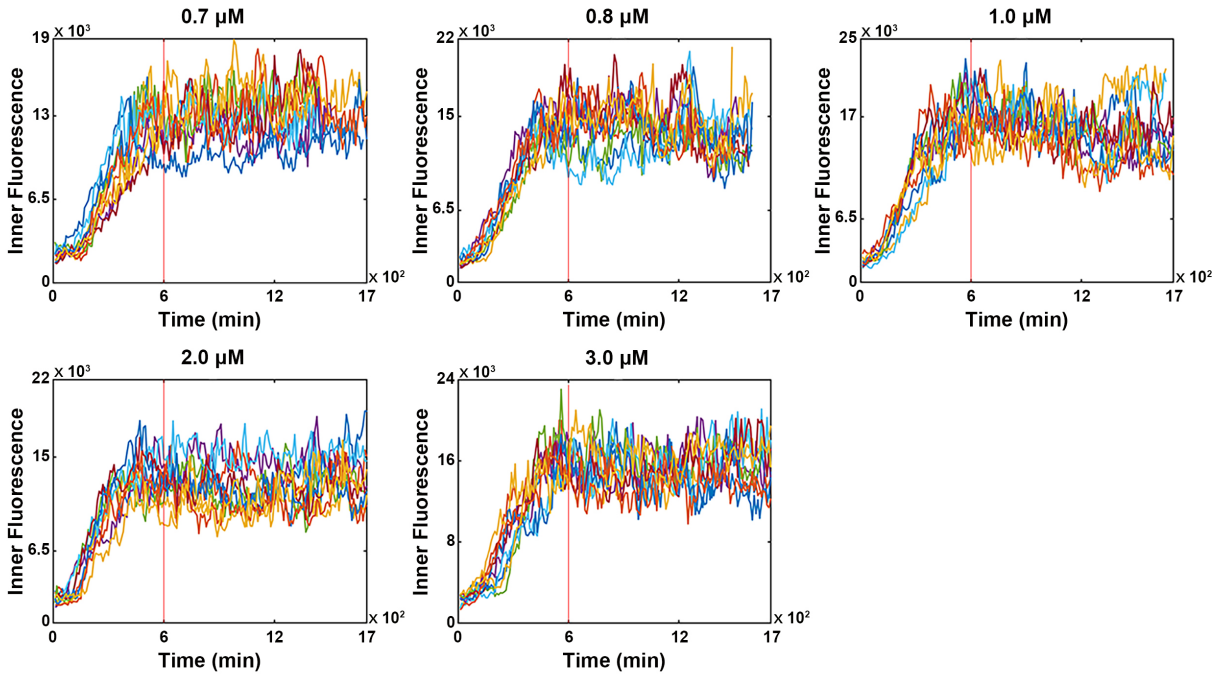

Fig. S1. The Partial fluorescence intensity trajectories of Fus3 inside the nucleus under the different pheromone doses. The red vertical line at 600 minutes is used to approximate the time node at which all cell fluorescence trajectories have entered a non-equilibrium steady state.

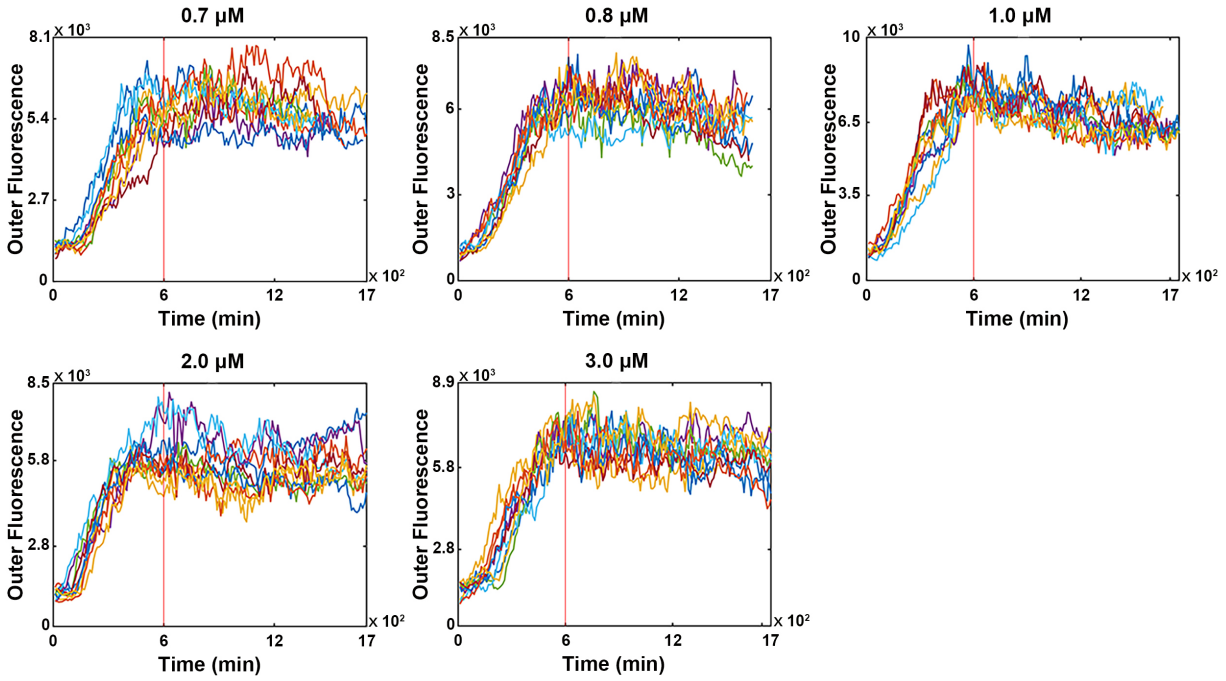

Fig. S2. The Partial fluorescence intensity trajectories of Fus3 outside the nucleus under the different pheromone doses. The red vertical line at 600 minutes is used to approximate the time node at which all cell fluorescence trajectories have entered a non-equilibrium steady state.

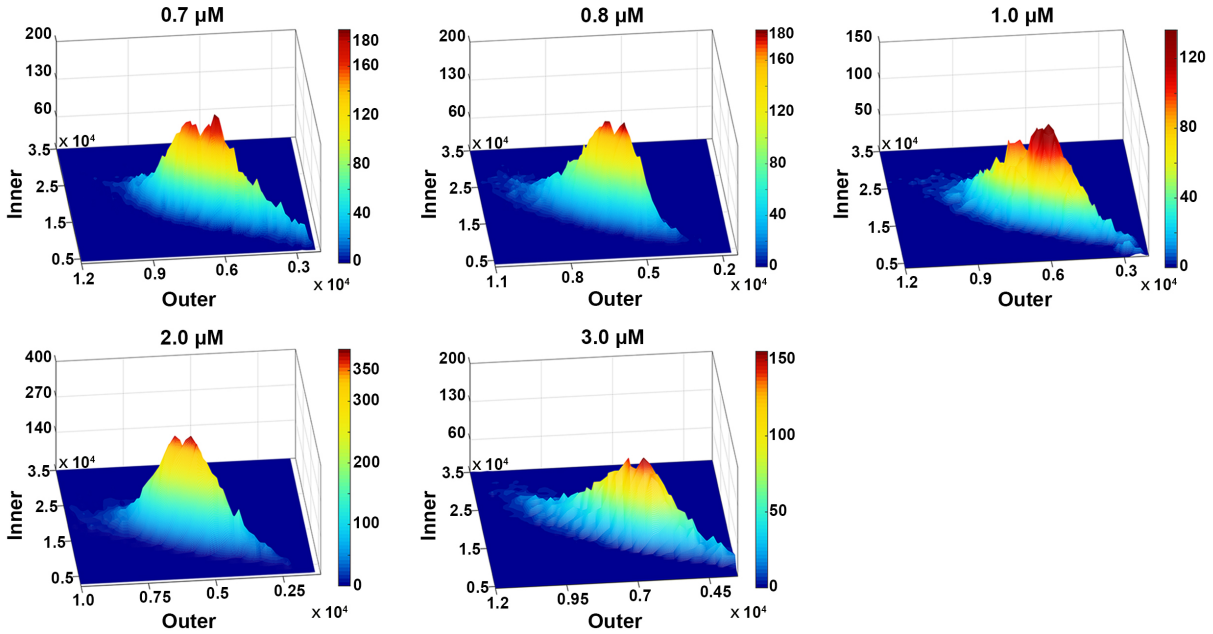

Fig. S3. The 3D distribution graph of Fus3 fluorescence intensity inside and outside the nucleus under the different pheromone doses.

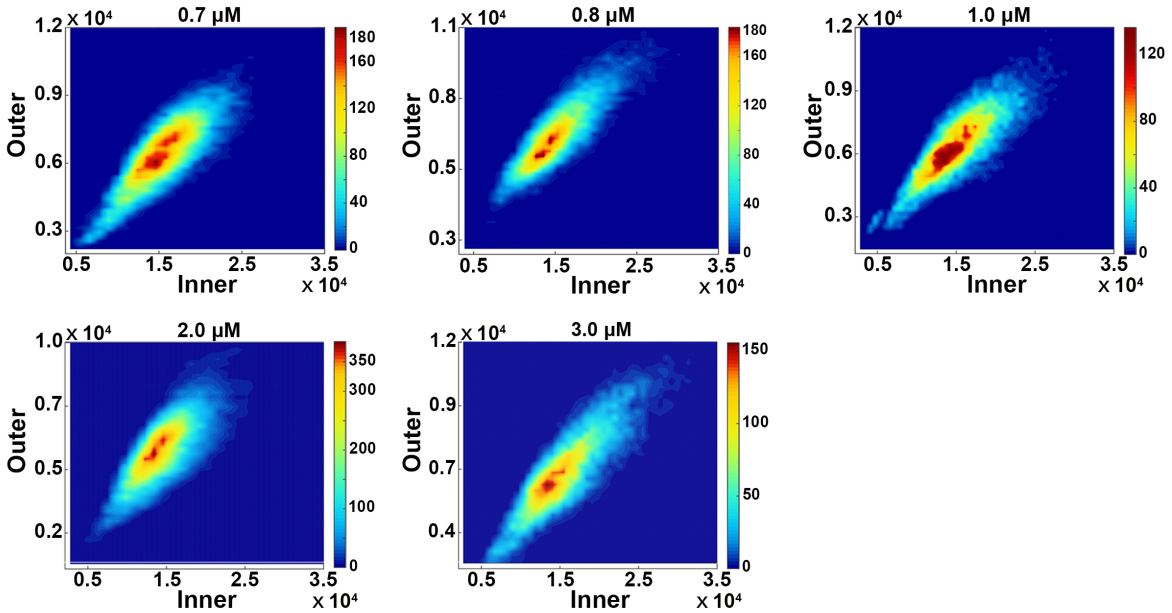

Fig. S4. The 2D distribution graph of Fus3 fluorescence intensity inside and outside the nucleus under the different pheromone doses.

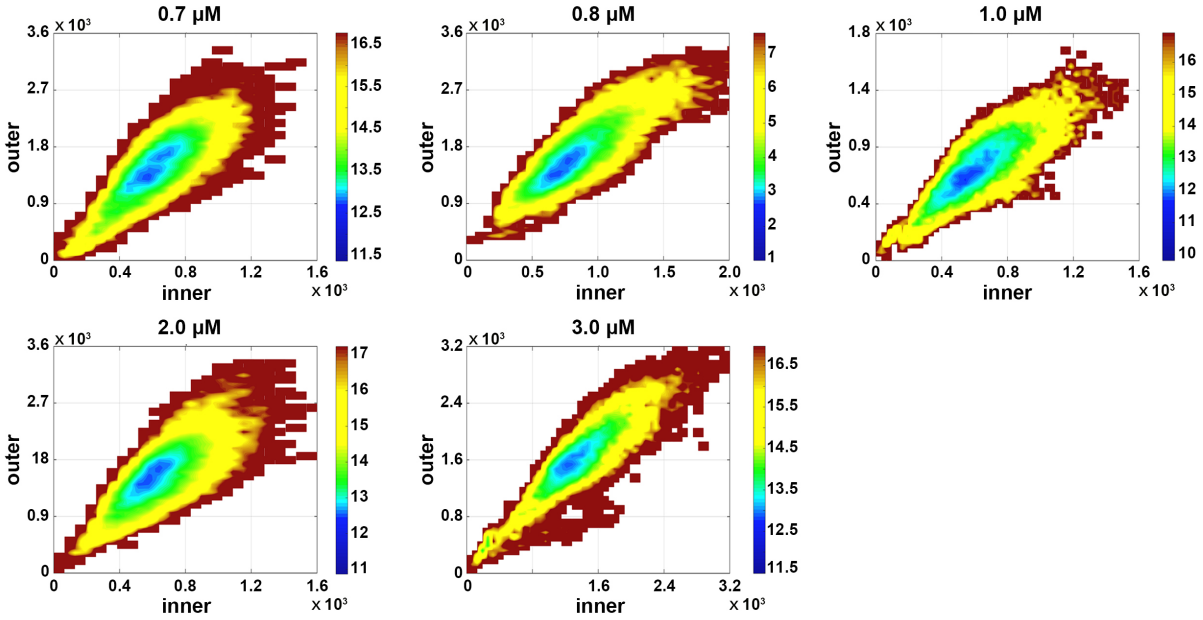

Fig. S5. The 2D underlying potential landscapes U under the different pheromone doses.

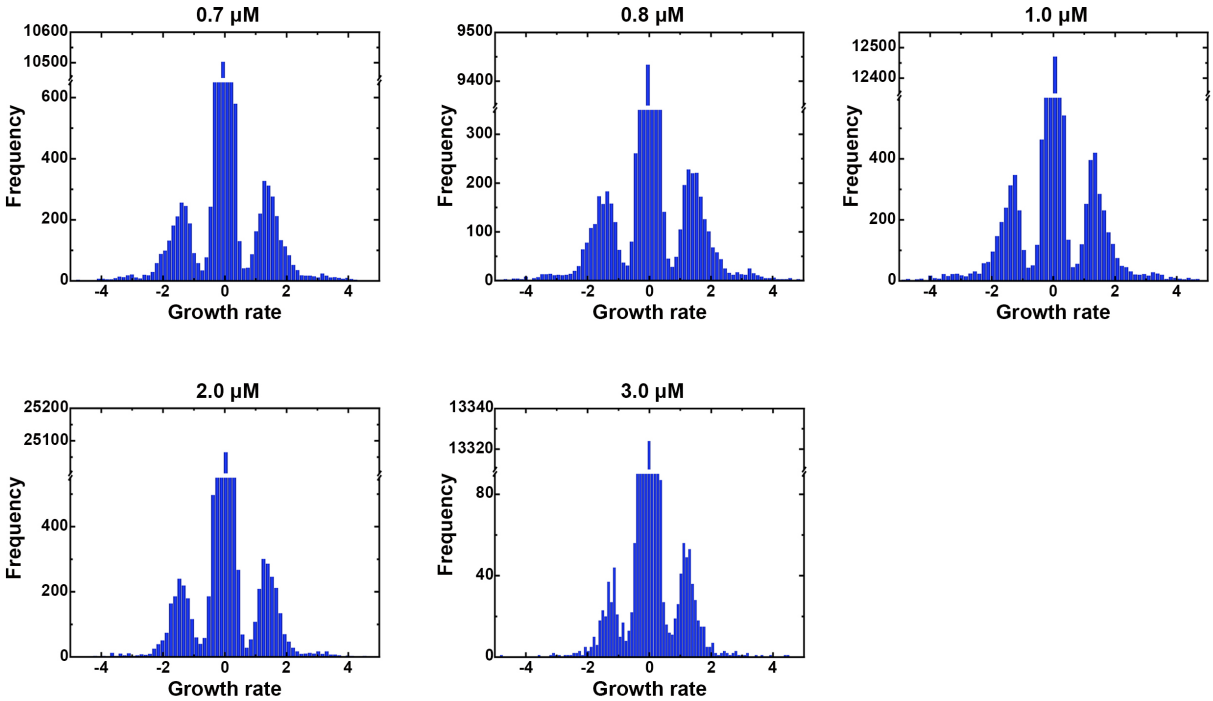

Fig. S6. Statistical graph of the cell growth rate under the different pheromone doses.

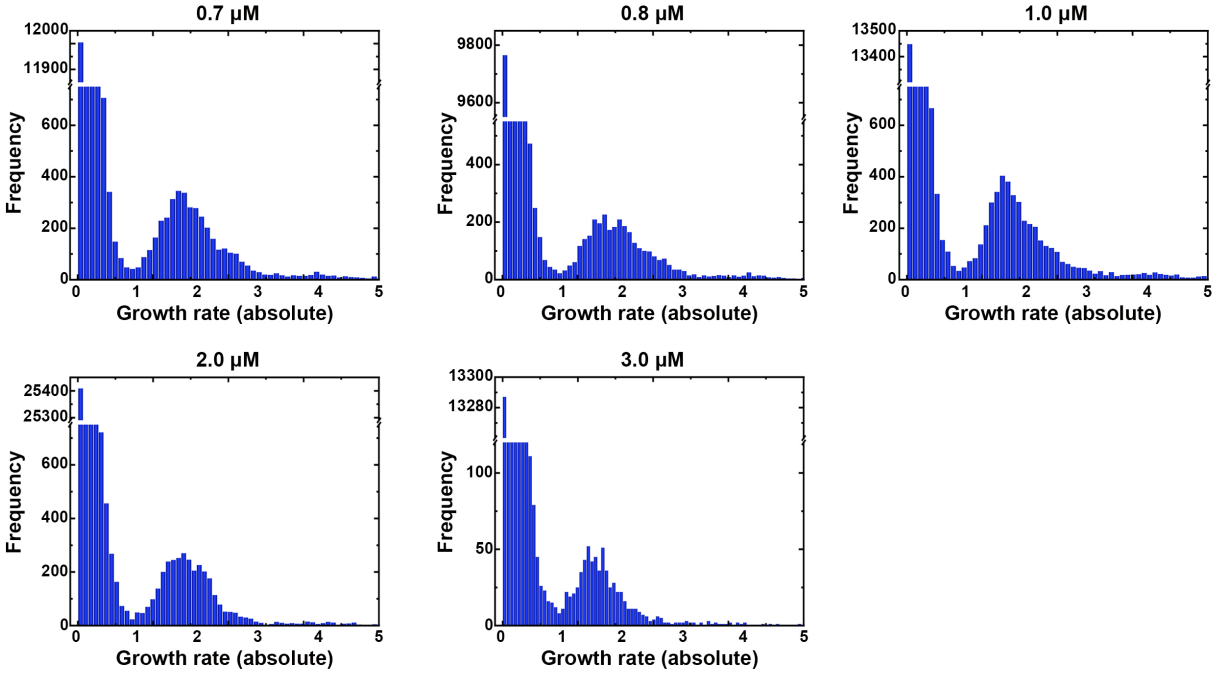

Fig. S7. Statistical graph depicting the absolute value of the cell growth rate at various pheromone concentrations.

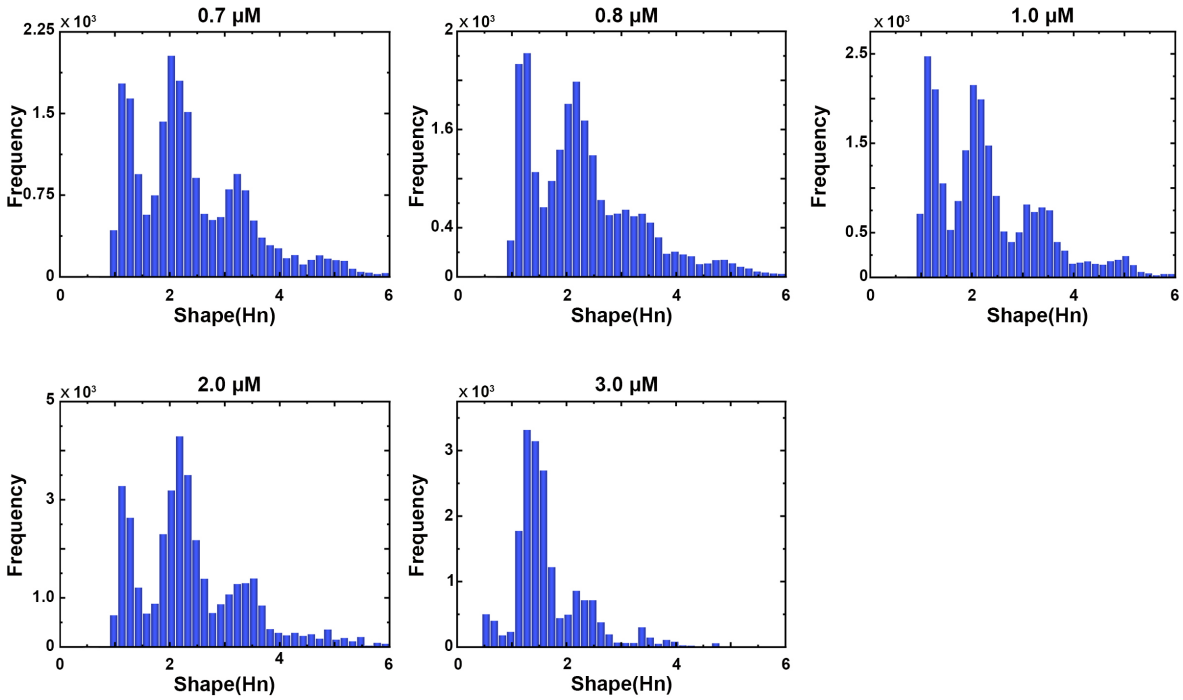

Fig. S8. The Statistical distribution of the cell morphological fates under the different pheromone doses.

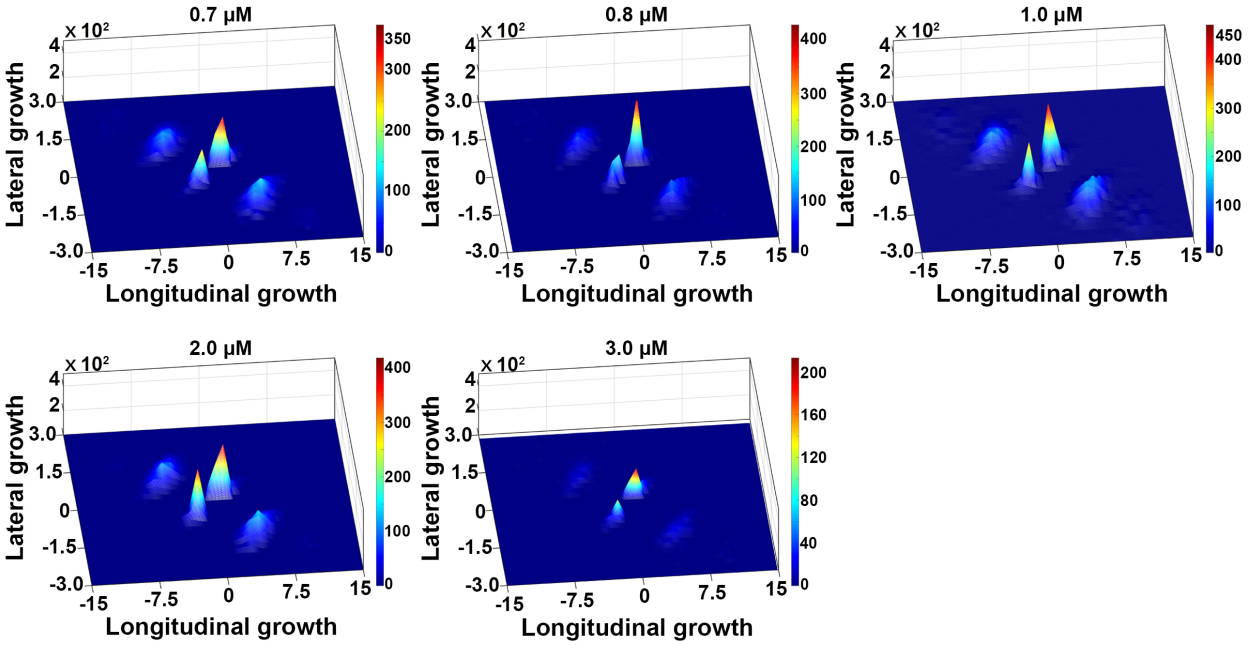

Fig. S9. The synergistic effect of both lateral and longitudinal cell growth capabilities at various pheromone concentrations. The x-axis represents the ability of cells to grow longitudinally, as indicated by the rate of change in the sum of the radii of the filled circles within the cells, i.e., $(R_1 + R_2 + \cdots + R_n)'$; the y-axis represents the ability of cells to grow laterally, as indicated by the rate of change in the average radius of the filled circles within the cells, i.e., $(\frac{R_1+R_2+\cdots+R_n}{n})'$.

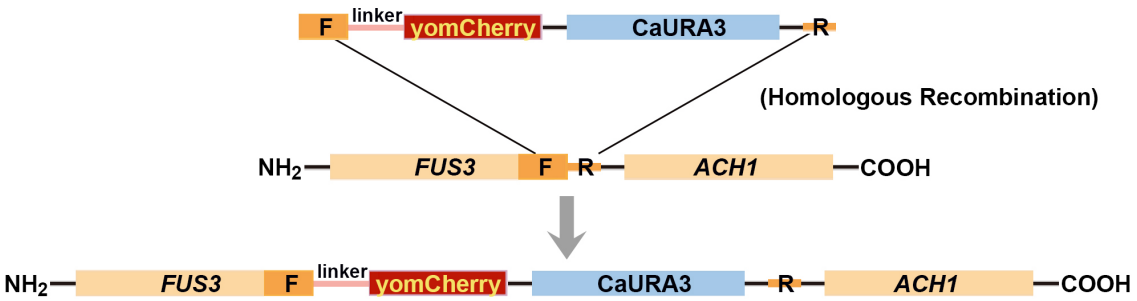

Fig. S10. Diagram illustrating the homologous recombination principle of *FUS3*-yomCherry. F/R is the left and right homology arms; the red fluorescent gene (yomCherry); the screening gene (CaURA3); the linker is a flexible chain (6aa [GS]x linker); Ach1 is the gene adjacent to the 3' end of *FUS3*.

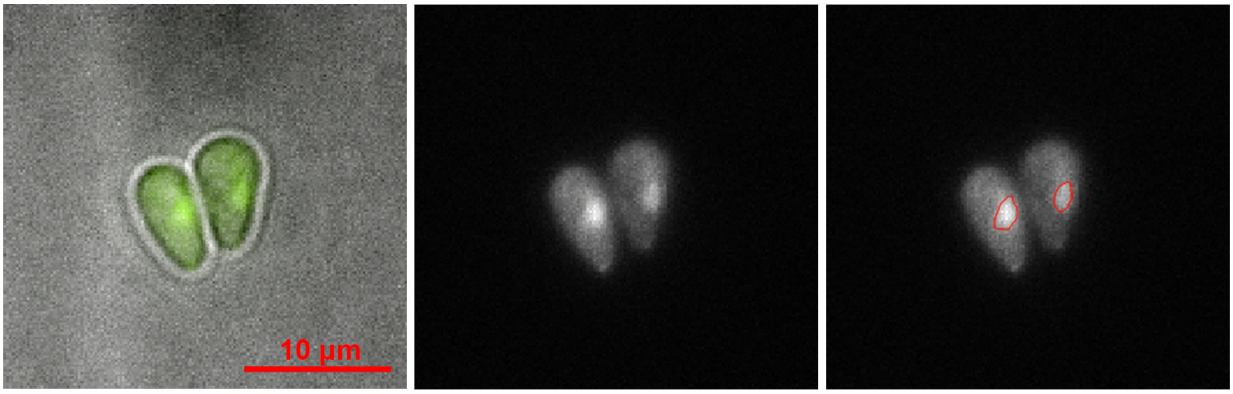

Fig. S11. Delineation of the cell nucleus's borders. The cells depicted in the image are yeast cells incubated with 0.7 uM pheromone for 280min; the GFP (S65T) linked to *FUS3* was excited by a 488 nm laser; the image on the left is a superposition of the fluorescence field and bright field, allowing the outline of yeast cells to be seen; the brightness of the images in the middle and on the right represents the gene expression level of Fus3; the red circles in the right panel depict the calculated nucleus boundaries.

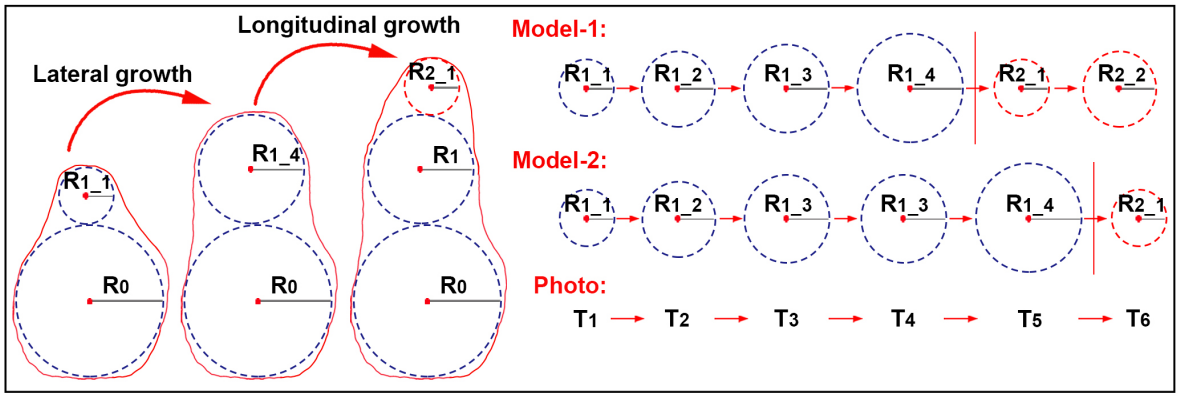

Fig. S12. Schematic illustration of two models of cell growth. R_0 is the maximum circle radius; R_1 is the minimum circle radius; the $(R_{1_1}), \ldots, (R_{1_4})$ are the radii of R_1 in the different growth stages; $(T_1, \ldots, T_6)$ are the times at which the microscope recorded the cell state.

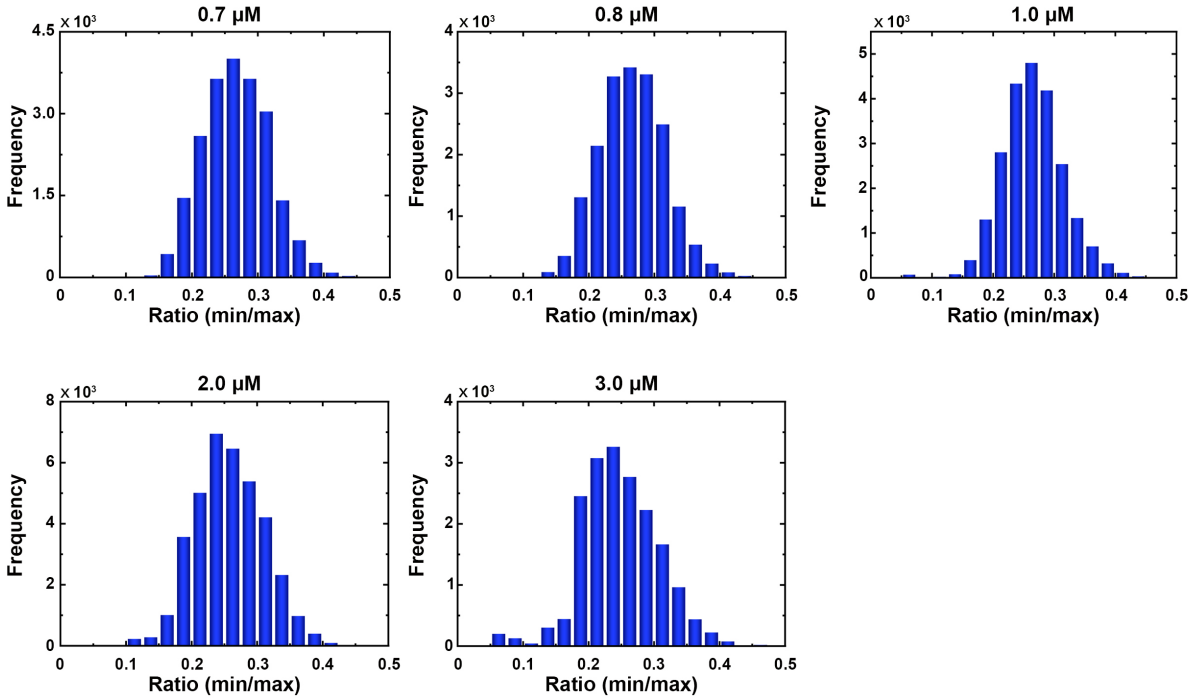

Fig. S13. The distribution diagram of the radius ratio between the smallest circle and the largest circle of the yeast cell shape under the different pheromone doses.

Table S1. The quantitative parameters in the net flux theory. Following the master equation, parameters of net flux are determined by fitting the real-time trajectories of cell morphology at 0.7 μM to hidden Markov chain models.

Pheromone dose (μM)	**0.7**
Number of transitions	$N_{(0.7\mu M)} = \begin{pmatrix} 13536 & 373 & 0 & 254 \\ 229 & 0 & 0 & 140 \\ 232 & 0 & 274 & 2834 \\ 64 & 0 & 3137 & 57 \end{pmatrix}$
Transition probability	$M_{(0.7\mu M)} = \begin{pmatrix} 0.9557 & 0.0263 & 0 & 0.0179 \\ 0.6206 & 0 & 0 & 0.3794 \\ 0.0695 & 0 & 0.0820 & 0.8485 \\ 0.0196 & 0 & 0.9629 & 0.0175 \end{pmatrix}$
Probability of the four states	$P_{(0.7\mu M)} = \begin{pmatrix} 0.6079 & 0.0160 & 0.1925 & 0.1835 \end{pmatrix}$
Asymmetric matrix	$C_{(0.7\mu M)} = \begin{pmatrix} 0 & 0.0030 & -0.0067 & 0.0036 \\ -0.0030 & 0 & 0 & 0.0030 \\ 0.0067 & 0 & 0 & -0.0067 \\ -0.0036 & -0.0030 & 0.0067 & 0 \end{pmatrix}$
Symmetric matrix	$D_{(0.7\mu M)} = \begin{pmatrix} 0.5810 & 0.0130 & 0.0067 & 0.0073 \\ 0.0130 & 0 & 0 & 0.0030 \\ 0.0067 & 0 & 0.0158 & 0.1700 \\ 0.0073 & 0.0030 & 0.1700 & 0.0032 \end{pmatrix}$
Net fluxes value	$J_{(0.7\mu M)} = \begin{pmatrix} J_1(\text{state1,state2,state3,state1}) = 0.0061 \\ J_2(\text{state1,state4,state3,state1}) = 0.0073 \\ J_3(\text{state2,state4,state3,state2}) = 0.0061 \end{pmatrix}$

Table S2. The quantitative parameters in the net flux theory. Following the master equation, parameters of net flux are determined by fitting the real-time trajectories of cell morphology at 0.8 μM to hidden Markov chain models.

Pheromone dose (μM)	**0.8**
Number of transitions	$N_{(0.8\mu M)} = \begin{pmatrix} 11957 & 328 & 0 & 140 \\ 218 & 4427 & 0 & 101 \\ 52 & 34 & 584 & 68 \\ 131 & 6 & 167 & 6 \end{pmatrix}$
Transition probability	$M_{(0.8\mu M)} = \begin{pmatrix} 0.9623 & 0.0264 & 0 & 0.0113 \\ 0.0459 & 0.9328 & 0 & 0.0213 \\ 0.0705 & 0.0461 & 0.7913 & 0.0921 \\ 0.4226 & 0.0194 & 0.5387 & 0.0194 \end{pmatrix}$
Probability of the four states	$P_{(0.8\mu M)} = \begin{pmatrix} 0.6447 & 0.2905 & 0.0467 & 0.0181 \end{pmatrix}$
Asymmetric matrix	$C_{(0.8\mu M)} = \begin{pmatrix} 0 & 0.0018 & -0.0016 & -0.0002 \\ -0.0018 & 0 & -0.0011 & 0.0029 \\ 0.0016 & 0.0011 & 0 & -0.0027 \\ 0.0002 & -0.0029 & 0.0027 & 0 \end{pmatrix}$
Symmetric matrix	$D_{(0.8\mu M)} = \begin{pmatrix} 0.6204 & 0.0152 & 0.0016 & 0.0075 \\ 0.0152 & 0.2709 & 0.0011 & 0.0033 \\ 0.0016 & 0.0011 & 0.0370 & 0.0070 \\ 0.0075 & 0.0033 & 0.0070 & 0.0004 \end{pmatrix}$
Net fluxes value	$J_{(0.8\mu M)} = \begin{pmatrix} J_1(\text{state1,state2,state3,state1}) = 0.0037 \\ J_2(\text{state1,state4,state3,state1}) = -0.0004 \\ J_3(\text{state2,state4,state3,state2}) = 0.0058 \end{pmatrix}$

Table S3. The quantitative parameters in the net flux theory. Following the master equation, parameters of net flux are determined by fitting the real-time trajectories of cell morphology at 1.0 μM to hidden Markov chain models.

Pheromone dose (μM)	**1.0**
Number of transitions	$N_{(1.0\mu M)} = \begin{pmatrix} 61 & 0 & 10956 & 41 \\ 0 & 0 & 24 & 0 \\ 10989 & 0 & 338 & 0 \\ 11 & 24 & 0 & 380 \end{pmatrix}$
Transition probability	$M_{(1.0\mu M)} = \begin{pmatrix} 0.0055 & 0 & 0.9908 & 0.0037 \\ 0 & 0 & 1.0000 & 0 \\ 0.9702 & 0 & 0.0298 & 0 \\ 0.0265 & 0.0578 & 0 & 0.9157 \end{pmatrix}$
Probability of the four states	$P_{(1.0\mu M)} = \begin{pmatrix} 0.4830 & 0.0012 & 0.4945 & 0.0212 \end{pmatrix}$
Asymmetric matrix	$C_{(1.0\mu M)} = 1.0e\text{-}03 * \begin{pmatrix} 0 & 0 & -0.6140 & 0.6140 \\ 0 & 0 & 0.6140 & -0.6140 \\ 0.6140 & -0.6140 & 0 & 0 \\ -0.6140 & 0.6140 & 0 & 0 \end{pmatrix}$
Symmetric matrix	$D_{(1.0\mu M)} = \begin{pmatrix} 0.0027 & 0 & 0.4792 & 0.0012 \\ 0 & 0 & 0.0006 & 0.0006 \\ 0.4792 & 0.0006 & 0.0148 & 0 \\ 0.0012 & 0.0006 & 0 & 0.0194 \end{pmatrix}$
Net fluxes value	$J_{(1.0\mu M)} = \begin{pmatrix} J_1(\text{state1,state2,state3,state1}) = 0.0000 \\ J_2(\text{state1,state4,state3,state1}) = -0.0012 \\ J_3(\text{state2,state4,state3,state2}) = -0.0012 \end{pmatrix}$

Table S4. The quantitative parameters in the net flux theory. Following the master equation, parameters of net flux are determined by fitting the real-time trajectories of cell morphology at 2.0 μM to hidden Markov chain models.

Pheromone dose (μM)	**2.0**
Number of transitions	$N_{(2.0\mu M)} = \begin{pmatrix} 67 & 0 & 0 & 1 \\ 2 & 96 & 59 & 2212 \\ 0 & 7 & 31075 & 474 \\ 0 & 2284 & 382 & 1 \end{pmatrix}$
Transition probability	$M_{(2.0\mu M)} = \begin{pmatrix} 0.9853 & 0 & 0 & 0.0147 \\ 0.0008 & 0.0405 & 0.0249 & 0.9337 \\ 0 & 0.0002 & 0.9848 & 0.0150 \\ 0 & 0.8564 & 0.1432 & 0.0004 \end{pmatrix}$
Probability of the four states	$P_{(2.0\mu M)} = \begin{pmatrix} 0.0040 & 0.0699 & 0.8480 & 0.0781 \end{pmatrix}$
Asymmetric matrix	$C_{(2.0\mu M)} = 1.0e\text{-}03 * \begin{pmatrix} 0 & -0.0295 & 0 & 0.0295 \\ 0.0295 & 0 & 0.7763 & -0.8058 \\ 0 & -0.7763 & 0 & 0.7763 \\ -0.0295 & 0.8058 & -0.7763 & 0 \end{pmatrix}$
Symmetric matrix	$D_{(2.0\mu M)} = \begin{pmatrix} 0.0040 & 0.0000 & 0 & 0.0000 \\ 0.0000 & 0.0028 & 0.0010 & 0.0661 \\ 0 & 0.0010 & 0.8351 & 0.0120 \\ 0.0000 & 0.0661 & 0.0120 & 0.0000 \end{pmatrix}$
Net fluxes value	$J_{(2.0\mu M)} = \begin{pmatrix} J_1(\text{state1,state2,state3,state1}) = \text{-}0.0001 \\ J_2(\text{state1,state4,state3,state1}) = \text{-}0.0001 \\ J_3(\text{state2,state4,state3,state2}) = \text{-}0.0016 \end{pmatrix}$

Table S5. The quantitative parameters in the net flux theory. Following the master equation, parameters of net flux are determined by fitting the real-time trajectories of cell morphology at 3.0 μM to hidden Markov chain models.

Pheromone dose (μM)	**3.0**
Number of transitions	$N_{(3.0\mu M)} = \begin{pmatrix} 0 & 0 & 0 & 870 \\ 0 & 13609 & 48 & 296 \\ 861 & 286 & 0 & 471 \\ 9 & 1 & 1628 & 48 \end{pmatrix}$
Transition probability	$M_{(3.0\mu M)} = \begin{pmatrix} 0 & 0 & 0 & 1.0000 \\ 0 & 0.9753 & 0.0034 & 0.0212 \\ 0.5321 & 0.1768 & 0 & 0.2911 \\ 0.0053 & 0.0006 & 0.9656 & 0.0285 \end{pmatrix}$
Probability of the four states	$P_{(3.0\mu M)} = \begin{pmatrix} 0.0552 & 0.7385 & 0.1027 & 0.1037 \end{pmatrix}$
Asymmetric matrix	$C_{(3.0\mu M)} = \begin{pmatrix} 0 & 0 & -0.0273 & 0.0273 \\ 0 & 0 & -0.0078 & 0.0078 \\ 0.0273 & 0.0078 & 0 & -0.0351 \\ -0.0273 & -0.0078 & 0.0351 & 0 \end{pmatrix}$
Symmetric matrix	$D_{(3.0\mu M)} = \begin{pmatrix} 0 & 0 & 0.0273 & 0.0279 \\ 0 & 0.7203 & 0.0103 & 0.0079 \\ 0.0273 & 0.0103 & 0 & 0.0650 \\ 0.0279 & 0.0079 & 0.0650 & 0.0030 \end{pmatrix}$
Net fluxes value	$J_{(3.0\mu M)} = \begin{pmatrix} J_1(\text{state1,state2,state3,state1}) = -0.0000 \\ J_2(\text{state1,state4,state3,state1}) = 0.0546 \\ J_3(\text{state2,state4,state3,state2}) = 0.0156 \end{pmatrix}$

Table S6. The description of the components in the biochemical reactions.

Name	Description
$G\mathrm{Fus3}$ or *FUS3*	The gene of the *FUS3*
$P\mathrm{Fus3}$ or Fus3	The protein of the *FUS3*
$P\mathrm{Fus3}_p$ or $\mathrm{Fus3}_p$	Phosphorylated protein of the *FUS3*
$(P\mathrm{Fus3}_p)'$ or $(\mathrm{Fus3}_p)'$	The $P\mathrm{Fus3}_p$ remaining after the chemical reaction
$P\mathrm{Fus3}_p$_inner	The $P\mathrm{Fus3}_p$ in the nucleus
$P\mathrm{Fus3}_p$_outer	The $P\mathrm{Fus3}_p$ outside the nucleus
$P\mathrm{Fus3}_p$_in	The $P\mathrm{Fus3}_p$ produced by the P_1 pathway in the nucleus
$P\mathrm{Fus3}_p$_out	The $P\mathrm{Fus3}_p$ produced by the P_2 pathway outside the nucleus
$P\mathrm{Fus3}$-B	This indicates the $P\mathrm{Fus3}_p$ produced by the action of the B
$G\mathrm{Fus3}$-self	The $G\mathrm{Fus3}$ produced by its self-activation
Φ	Protein degradation

342 **Table S7. The list of the components in the biochemical reactions.**

1	*G*Fus3	**21**	*G*Fus3-*P*Msg5p
2	(*G*Fus3)'	**22**	(*G*Fus3-*P*Msg5p)'
3	*P*Fus3p_outer	**23**	*G*Far1
4	*pheromone*	**24**	(*G*Far1)'
5	*G*Fus3-pheromone	**25**	*P*Far1p
6	(*G*Fus3-pheromone)'	**26**	*G*Far1p-*P*Fus3p_inner
7	*G*Fus3-self	**27**	(*G*Far1-*P*Fus3p_inner)'
8	(*G*Fus3-self)'	**28**	*G*Bni1
9	*P*Fus3p_inner	**29**	(*G*Bni1)'
10	∅	**30**	*P*Bni1p
11	*G*Ste12	**31**	*G*Fus3_outer-*P*Bni1p
12	(*G*Ste12)'	**32**	(*G*Fus3_outer-*P*Bni1p)'
13	*P*Ste12p	**33**	*G*Bni1_in
14	*G*Ste12-*P*Fus3p_inner	**34**	*G*Bni1_in-*P*Far1p
15	(*G*Ste12-*P*Fus3p_inner)'	**35**	(*G*Bni1_in-*P*Far1p)'
16	*G*Msg5	**36**	*P*Bni1p_in
17	(*G*Msg5)'	**37**	*G*Bni1_out
18	*P*Msg5p	**38**	*G*Bni1_out-*P*Fus3p_outer
19	*G*Msg5-*P*Ste12p	**39**	(*G*Bni1_out-*P*Fus3p_outer)'
20	(*G*Msg5-*P*Ste12p)'	**40**	*P*Bni1p_out

343
344

Table S8. The list of the biochemical reactions.

1	$G\text{Fus3} \xrightarrow{k_1=1} (G\text{Fus3})' + (P\text{Fus3p_outer})$
2	$G\text{Fus3} + \textit{pheromone} \xrightarrow{k_2=0.7} (G\text{Fus3-pheromone})$
3	$(G\text{Fus3-pheromone}) \xrightarrow{k_3=0.001} G\text{Fus3} + \textit{pheromone}$
4	$(G\text{Fus3-pheromone}) \xrightarrow{k_4=1.5} (G\text{Fus3-pheromone})' + (P\text{Fus3p_outer})$
5	$G\text{Fus3} + (P\text{Fus3p_outer}) \xrightarrow{k_5=0.7} (G\text{Fus3-self})$
6	$(G\text{Fus3-self}) \xrightarrow{k_6=0.001} G\text{Fus3} + (P\text{Fus3p_outer})$
7	$(G\text{Fus3-self}) \xrightarrow{k_7=1.5} (G\text{Fus3-self})' + (P\text{Fus3p_outer})$
8	$(P\text{Fus3p_outer}) \xrightarrow{k_8=3.7} (P\text{Fus3p_inner})$
9	$(P\text{Fus3p_inner}) \xrightarrow{k_9=3.7} (P\text{Fus3p_outer})$
10	$(P\text{Fus3p_outer}) \xrightarrow{k_{10}=0.01} \varnothing$
11	$(P\text{Fus3p_inner}) \xrightarrow{k_{11}=0.01} \varnothing$
12	$G\text{Ste12} \xrightarrow{k_{12}=1} (G\text{Ste12})' + P\text{Ste12p}$
13	$G\text{Ste12} + (P\text{Fus3p_inner}) \xrightarrow{k_{13}=0.7} (G\text{Ste12-}P\text{Fus3p_inner})$
14	$(G\text{Ste12-}P\text{Fus3p_inner}) \xrightarrow{k_{14}=0.001} G\text{Ste12} + (P\text{Fus3p_inner})$
15	$(G\text{Ste12-}P\text{Fus3p_inner}) \xrightarrow{k_{15}=1.5} (G\text{Ste12-}P\text{Fus3p_inner})' + P\text{Ste12p}$
16	$G\text{Msg5} \xrightarrow{k_{16}=1} (G\text{Msg5})' + P\text{Msg5p}$
17	$G\text{Msg5} + P\text{Ste12p} \xrightarrow{k_{17}=0.7} (G\text{Msg5-}P\text{Ste12p})$
18	$(G\text{Msg5-}P\text{Ste12p}) \xrightarrow{k_{18}=0.001} G\text{Msg5} + P\text{Ste12p}$
19	$(G\text{Msg5-}P\text{Ste12p}) \xrightarrow{k_{19}=1.2} (G\text{Msg5-}P\text{Ste12p})' + P\text{Msg5p}$
20	$G\text{Fus3} + P\text{Msg5p} \xrightarrow{k_{20}=0.7} (G\text{Fus3-}P\text{Msg5p})$
21	$(G\text{Fus3-}P\text{Msg5p}) \xrightarrow{k_{21}=0.001} G\text{Fus3} + P\text{Msg5p}$
22	$(G\text{Fus3-}P\text{Msg5p}) \xrightarrow{k_{22}=0.5} (G\text{Fus3-}P\text{Msg5p})' + (P\text{Fus3p_outer})$
23	$(P\text{Ste12p}) \xrightarrow{k_{23}=0.01} \varnothing$
24	$(P\text{Msg5p}) \xrightarrow{k_{24}=0.01} \varnothing$
25	$G\text{Far1} \xrightarrow{k_{25}=1} (G\text{Far1})' + P\text{Far1p}$
26	$G\text{Far1} + (P\text{Fus3p_inner}) \xrightarrow{k_{26}=0.7} (G\text{Far1p-}P\text{Fus3p_inner})$
27	$(G\text{Far1p-}P\text{Fus3p_inner}) \xrightarrow{k_{27}=0.001} G\text{Far1} + (P\text{Fus3p_inner})$
28	$(G\text{Far1-}P\text{Fus3p_inner}) \xrightarrow{k_{28}=1.5} (G\text{Far1-}P\text{Fus3p_inner})' + (P\text{Far1p})$
29	$(P\text{Far1p}) \xrightarrow{k_{29}=0.01} \varnothing$
30	$G\text{Bni1} \xrightarrow{k_{30}=0.1} (G\text{Bni1})' + P\text{Bni1p}$

31	$G\text{Fus3_outer} + P\text{Bni1p} \xrightarrow{k_{31}=0.7} (G\text{Fus3_outer-}P\text{Bni1p})$
32	$(G\text{Fus3_outer-}P\text{Bni1p}) \xrightarrow{k_{32}=0.001} G\text{Fus3_outer} + P\text{Bni1p}$
33	$(G\text{Fus3_outer-}P\text{Bni1p}) \xrightarrow{k_{33}=0.5} (G\text{Fus3_outer-}P\text{Bni1p})' + (P\text{Fus3p_outer})$
34	$(G\text{Bni1_in}) + P\text{Far1p} \xrightarrow{k_{34}=0.7} (G\text{Bni1_in-}P\text{Far1p})$
35	$(G\text{Bni1_in-}P\text{Far1p}) \xrightarrow{k_{35}=0.7} (G\text{Bni1_in}) + P\text{Far1p}$
36	$(G\text{Bni1_in-}P\text{Far1p}) \xrightarrow{k_{36}=1.5} (G\text{Bni1_in-}P\text{Far1p})' + (P\text{Bni1p_in})$
37	$(G\text{Bni1_out}) + (P\text{Fus3p_outer}) \xrightarrow{k_{37}=0.7} (G\text{Bni1_out-}P\text{Fus3p_outer})$
38	$(G\text{Bni1_out-}P\text{Fus3p_outer}) \xrightarrow{k_{38}=0.7} (G\text{Bni1_out}) + (P\text{Fus3p_outer})$
39	$(G\text{Bni1_out-}P\text{Fus3p_outer}) \xrightarrow{k_{39}=1.5} (G\text{Bni1_out-}P\text{Fus3p_outer})' + (P\text{Bni1p_out})$
40	$(P\text{Bni1p_out}) \xrightarrow{k_{40}=0.01} \varnothing$
41	$(P\text{Bni1p_in}) \xrightarrow{k_{41}=0.01} \varnothing$

349 **Table S9. The components of the homologous recombination vector.**

Name	Sequence
homologous long arms F' (300 bp)	CCCAGGGCTAGAGAGTACATAAAGTCGCTTCCCATGTACCCTGCCGCGCCACTGGAGAAGATGTTCCCTCGAGTCAACCCGAAAGGCATAGATCTTTTACAGCGTATGCTTGTTTTTGACCCTGCGAAGAGGATTACTGCTAAGGAGGCACTGGAGCATCCGTATTTGCAAACATACCACGATCCAAACGACGAACCTGAAGGCGAACCCATCCCACCCAGCTTCTTCGAGTTTGATCACTACAAGGAGGCACTAACGACGAAAGACCTCAAGAAACTCATTTGGAACGAAATATTTAGT
homologous long arms R' (300 bp)	CCATCATTATCATTAAAATATCAACCCGAAGAACAATGTATACATATACATATACGTACACATATACATATGTACATATGACATACGTATTAGCCGCTGAGGACGCGGACGTATAAAAGGACAATACTTATATGGAGCTAAGGGGAGCAGTTACGCAACTCCGTGATCGCGCGCCACGGGCCGTCGGCGGCTGTTAATTGAAGAAAAAAAAAATGAAGAACCACAAGGGGTGATCCATATAGGTGACTAGCATCATCCCCTGCGACGCGCGGCCCGCCGGGCCAAAGGCGGGCAATGCGC
6aa [GS]x linker (18 bp)	ggtagcggcagcggtagc
Primer F (20 bp)	AAGTCGCTTCCCATGTACCC
Primer R (20 bP)	GTTGCGTAACTGCTCCCCTT

350

Movies S1-S7: Total internal reflection microscopy images of yeast cell (*FUS3*-GFP strain) in response to 0.2 μM, 0.6 μM, 0.7 μM, 0.8 μM, 1.0 μM, 2.0 μM, and 3.0 μM pheromone over time. The shooting interval of the photos was 10 minutes/frame. Yeast cells were cultured in a microfluidic device containing the normal YNB medium for 60 minutes, and then switched to the medium containing a specific concentration of pheromone for cultivation. The green fluorescence in the cell is the gene expression level of Fus3.

Movies S8-S9: Total internal reflection microscopy images of yeast cells (*CDC24*_GFP-*FUS3*_yomCherry strain) in response to 0.8 μM pheromone over time. The shooting interval of the photos was 10 minutes/frame. Yeast cells were cultured in a microfluidic device containing the normal YNB medium for 60 minutes, and then switched to the medium containing a specific concentration of pheromone for cultivation. The green fluorescence in the cell is the gene expression level of Cdc24; the red fluorescence in the cell is the gene expression level of Fus3.

References:

1. P. M. P. Anne-Christine Butty, Linda S. Huang, Ira Herskowitz, Matthias Peter*, The Role of Far1p in Linking the Heterotrimeric G Protein to Polarity Establishment Proteins During Yeast Mating. *SCIENCE*, (1998).
2. D. Matheos, M. Metodiev, E. Muller, D. Stone, M. D. Rose, Pheromone-induced polarization is dependent on the Fus3p MAPK acting through the formin Bni1p. *The Journal of cell biology* **165**, 99-109 (2004).
3. M. Peter, A. Gartner, J. Horecka, G. Ammerer, I. Herskowitz, FAR1 links the signal transduction pathway to the cell cycle machinery in yeast. *Cell* **73**, 747-760 (1993).
4. E. Elion, B. Satterberg, J. Kranz, FUS3 phosphorylates multiple components of the mating signal transduction cascade: evidence for STE12 and FAR1. *Molecular biology of the cell* **4**, 495-510 (1993).
5. R. L. Roberts, G. R. Fink, Elements of a single MAP kinase cascade in Saccharomyces cerevisiae mediate two developmental programs in the same cell type: mating and invasive growth. *Genes & development* **8**, 2974-2985 (1994).
6. I. Herskowitz, MAP kinase pathways in yeast: for mating and more. *Cell* **80**, 187-197 (1995).
7. E. A. Elion, J. A. Brill, G. R. Fink, FUS3 represses CLN1 and CLN2 and in concert with KSS1 promotes signal transduction. *Proceedings of the National Academy of Sciences* **88**, 9392-9396 (1991).
8. E. Blackwell *et al.*, Effect of the pheromone-responsive Gα and phosphatase proteins of Saccharomyces cerevisiae on the subcellular localization of the Fus3 mitogen-activated protein kinase. *Molecular and cellular biology* **23**, 1135-1150 (2003).
9. F. van Drogen, V. M. Stucke, G. Jorritsma, M. Peter, MAP kinase dynamics in response to pheromones in budding yeast. *Nature cell biology* **3**, 1051-1059 (2001).
10. A. Papagiannakis, B. Niebel, E. C. Wit, M. Heinemann, Autonomous Metabolic Oscillations Robustly Gate the Early and Late Cell Cycle. *Mol Cell* **65**, 285-295 (2016).
11. F. Caudron, Y. Barral, A super-assembly of Whi3 encodes memory of deceptive encounters by single cells during yeast courtship. *Cell* **155**, 1244-1257 (2013).
12. A. Doncic *et al.*, Compartmentalization of a bistable switch enables memory to cross a feedback-driven transition. *Cell* **160**, 1182-1195 (2015).